

Long-lived magnetization in an atomic spin chain tuned to a diabolic point

R.J.G. Elbertse¹, D. Borodin², J. Oh^{2,3}, T. Ahn^{2,3}, J. Hwang^{2,3}, J.C. Rietveld¹,
A.J. Heinrich^{2,3}, F. Delgado^{4*}, S. Otte^{1*}, Y. Bae^{2,3*†}

¹*Department of Quantum Nanoscience, Kavli Institute of Nanoscience,
Delft University of Technology, Delft, The Netherlands*

²*Center for Quantum Nanoscience, Institute for Basic Science (IBS), Seoul, South Korea*

³*Department of Physics, EWha Womans University, Seoul, South Korea*

⁴*Instituto Universitario de Estudios Avanzados IUDEA, Departamento de Física, Universidad de La Laguna
La Laguna, Tenerife, Spain*

[†]*Current address: Empa, Swiss Federal Laboratories for Materials Science and Technology,
nanotech@surfaces Laboratory, Switzerland*

(Dated: July 4, 2024)

Scaling magnets down to where quantum size effects become prominent triggers quantum tunneling of magnetization (QTM), profoundly influencing magnetization dynamics. Measuring magnetization switching in an Fe atomic chain under a carefully tuned transverse magnetic field, we observe a non-monotonic variation of magnetization lifetimes around a level crossing, known as the diabolic point (DP). Near DPs, local environment effects causing QTM are efficiently suppressed, enhancing lifetimes by three orders of magnitude. Adjusting interatomic interactions further facilitates multiple DPs. Our study provides a deeper understanding of quantum dynamics near DPs and enhances our ability to engineer a quantum magnet.

In quantum mechanical systems, unusual dynamic processes occur when energy levels approach and mix with each other. In a two-parameter space, the degeneracy between orthogonal states creates a level crossing of energy surfaces (Fig. 1a), the shape of which reminds of the toy, *diabolo*, and thus is dubbed a diabolic point (DP) [1]. This DP has attracted significant attention in quantum magnets [2], which are characterized by two metastable magnetization states separated by an energy barrier [3, 4]. In the vicinity of the DP, quantum tunneling of magnetization (QTM) between these states is suppressed due to destructive interference among separate tunneling paths [5–7]. While the importance of DPs has been shown from ensembles of molecular magnets [2, 8, 9], precise control of local environments as a control knob of DPs has remained elusive.

Manipulation of magnetic atoms with a scanning tunneling microscope (STM) allows for the assembly of prototypical quantum magnets with controllable energy barriers ranging from 100 μeV to 100 meV [10–12]. The lifetime of magnetization states in these magnets can be determined by monitoring the spin polarized current through one of the magnet’s atoms over time [13]. When the magnetic anisotropy barrier exceeds the thermal energy, the lifetime is dominated by through-the-barrier transitions, i.e. QTM, resulting from hybridization between quantum states on either side of the barrier. While various systems have been studied with different degree of spin state hybridization [13] and spin-spin interactions [13, 14], it remains challenging to vary individual parameters due to the discrete nature of binding sites on surfaces. Instead, a more effective control knob for QTM may be achieved by exploiting the physics of a DP, where the hybridization of the quantum states is expected to

quench, allowing, at least in principle, arbitrarily long lifetimes.

In this work, we demonstrate the manifestation of DPs through the spin dynamics of nanomagnets by assembling Fe atoms into chains on $\text{Cu}_2\text{N}/\text{Cu}(100)$. Precisely adjusting chain length and interatomic spacing enables us to tailor the spin-spin interactions and thereby to engineer DPs in a controlled manner. When tuning the direction and strength of the external magnetic field near a DP, we observed a significant increase of magnetic lifetimes, with enhancement of up to three orders of magnitude. We provide a comprehensive picture of the quantum state composition near the DP, offering a rational strategy to control the spin dynamics of quantum magnets.

To model a chain of N Fe atoms on Cu-sites of Cu_2N , we consider a spin Hamiltonian that includes the Zeeman energy, the uniaxial and transverse magnetic anisotropy terms for each atom, as well as the Heisenberg exchange interaction between neighboring atoms [13, 15–17]:

$$H = \sum_i^N [g_i \mu_B \mathbf{B}_i^{\text{tot}} \cdot \mathbf{S}_i + D_i S_{i,z}^2 + E_i (S_{i,x}^2 - S_{i,y}^2)] + \sum_i^{N-1} J_i \mathbf{S}_i \cdot \mathbf{S}_{i+1}. \quad (1)$$

For an Fe atom on site i , $\mathbf{B}_i^{\text{tot}} = \mathbf{B} + \mathbf{B}_i^{\text{tip}}$ is the total magnetic field composed of external and tip fields, μ_B the Bohr magneton, and \mathbf{S}_i the spin operator with a magnitude of $S_i = 2$. Note that we allow for subtle variations in the values of the g-factor g_i , anisotropy parameters D_i and E_i , and exchange interaction strength J_i between atoms in the chain, since these parameters might vary due to subtle changes in the local strain in the underlying Cu_2N layer, as evidenced by variations of

Hamiltonian parameters throughout the literature (see Table S1). The easy-axis z is oriented along the in-plane Cu-N bonds [10]; we define the x and y axes as the remaining in-plane direction and the out-of-plane direction, respectively (Fig. 1b). Since the chain is not perfectly aligned with the external magnetic field in the experiment, the angle α is used to decompose the external field into both transverse (B_x) and longitudinal (B_z) components.

We investigate the DPs as a function of the transverse magnetic field, B_x . Solving the spin Hamiltonian (Eq. 1) for a single Fe atom ($N = 1$) gives the analytical solution for the $B_{x,n}$ fields where the DPs appear [18, 19]:

$$B_{x,n} = \frac{n\sqrt{2E(E-D)}}{g\mu_B}. \quad (2)$$

Here, n is the diabolic point index that ranges from $2S-1$ to $1-2S$ in double-integer steps. To estimate the location of DPs, we use Hamiltonian parameters which have been obtained from previous work, see Supplementary Note 1. For a single Fe atom at the Cu site, the lowest positive magnetic field DP ($n = 1$) is expected at $B_{x,1} \approx 9.5$ T. A second DP ($n = 3$) can be reached at even larger values of B_x . As depicted in Fig. 1a, when $B_x = B_{x,1}$ and $B_z = 0$, an energy level crossing occurs between the two lowest-lying eigenstates, ψ_0 and ψ_1 . When a small B_z is applied, sweeping B_x results in an avoided level crossing, as shown by the surface cut in Fig. 1a.

Diabolic points in atomic chains of length $N > 1$ with $|J/D| \lesssim 1$ can be understood in a similar fashion, although there are now N diabolic points for each diabolic point index, leading to a total of $2NS$ diabolic points. Now, the spin-spin interaction between the atoms can be used as a control knob for the location of DPs as a function of B_x . By adjusting the number of atoms in the chain and the interatomic distance, we are able to precisely determine the magnetic field values at which DPs are expected to occur (see Supplementary Note 2).

The magnetic fields needed to identify the DP in a single Fe atom are beyond available transverse magnetic field (6 T) of our instrument [10, 19]. However, for longer chains, the DP eventually becomes accessible within the range of our experimental capabilities. Our initial calculations using Eq. 1 predicted a DP for an antiferromagnetically coupled Fe_5 chain (Fig. 1b) at $B_{x,1} \sim 4$ T (see Supplementary Note 2), which guided our spin lifetime measurements. We investigate the influence of DPs on the magnetization bistability of the Fe atomic chains with spin-polarized STM.

Figure 1c schematically shows the energy levels of the two lowest-lying states (ψ_0 and ψ_1) in the antiferromagnetic Fe_5 chain as a function of transverse magnetic fields. For $B_x \ll B_{x,1}$, these two states are mainly composed of Néel states, denoted as $N_A = \{-2, +2, -2, +2, -2\}$ and $N_B = \{+2, -2, +2, -2, +2\}$ (expressed in the S_z -basis),

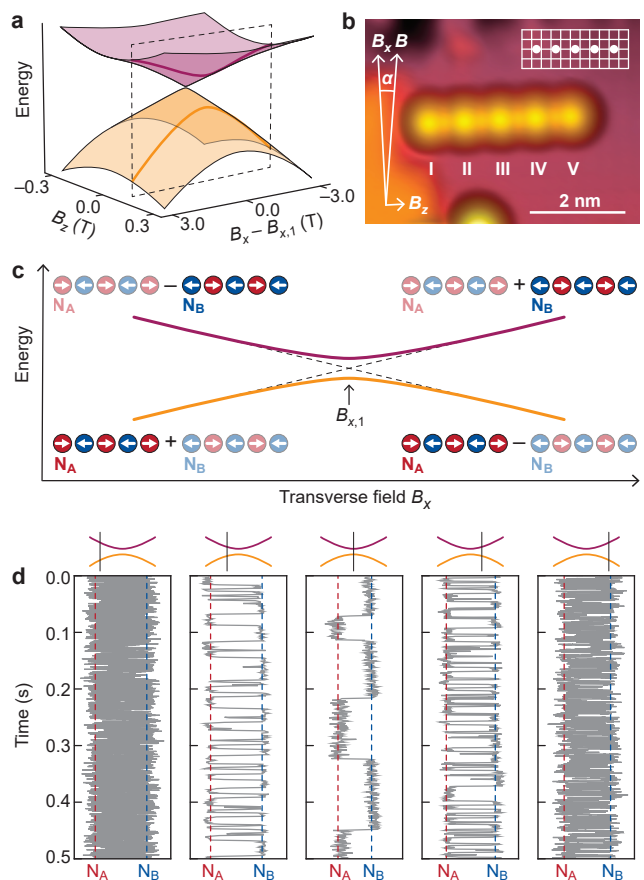


FIG. 1. Diabolic points in Fe atomic chains on Cu_2N . (a) Energy levels for the two lowest states of a single Fe atom (orange for the ground state ψ_0 and pink for the first-excited state ψ_1) with a diabolic point at the crossing. Thick lines show a cut of the energy surfaces, indicating the corresponding energies of the two states at a finite B_z outlined by the dashed rectangle. (b) Constant-current STM image of a Fe_5 chain ($V_{\text{DC}} = 100$ mV, $I = 10$ pA, $B_x = 2$ T). Atoms are labeled in Roman numerals (I-V). Schematics shows Fe atoms (white circles) on top of Cu_2N lattice. The intersections of grid lines correspond to the nitrogen atom position in Cu_2N . Magnetic field directions are tilted by the angle α with respect to the crystal axis. (c) Schematic overview of state composition for ψ_0 and ψ_1 of Fe_5 along a similar cut as in panel a. (d) Current traces taken for atom III of antiferromagnetically coupled Fe_5 and different magnetic fields around the DP, located at 4.2 T, indicated in the schematics above. Unless stated otherwise, all traces are obtained at 3 mV and approximately 10 pA, where magnetization switching occurs due to QTM and over-the-barrier excitation can be neglected, see Supplementary Note 8 for further details.

with subtle contributions from other spin states. Owing to the presence of a finite longitudinal component of the field and N being an odd number, the ground state ψ_0 has a larger contribution from N_A ($> 98\%$) compared to N_B , while the opposite holds for ψ_1 . The finite contributions of both N_A and N_B in these two states demonstrate

that the Néel states are hybridized, enabling QTM between them.

In ψ_0 , the contributions of N_A and N_B are symmetric, whereas in ψ_1 they are antisymmetric. Around $B_x = B_{x,1}$, the two states undergo an avoided level crossing, beyond which their symmetry is inverted. At the DP, the contribution of the minority Néel state vanishes, significantly enhancing the purity of ψ_0 and ψ_1 as mainly composed of N_A and N_B , respectively, thereby suppressing QTM.

Using spin-polarized STM, we are able to capture the time-dependent magnetization switching of the Fe chain at different B_x . By positioning the tip above one of the Fe atoms in the chain, we observe telegraph noise in the current signals, arising from the magnetization switching between the two lowest-lying states of the chain (Fig. 1d). The specific spin polarization of the tip, and which atom in the chain is being probed, determines the current value characteristic for N_A and N_B . For $B_x \ll B_{x,1}$, we detect rapid, yet clearly distinguishable switching events between two distinct current values. As B_x approaches the DP, the switching rate markedly decreases, to gradually increase again beyond the DP.

To quantitatively investigate the evolution of spin dynamics around the DPs, we extract the values of spin lifetimes from a current trace as demonstrated in Fig. 2a. Shown are the lifetimes τ_A and τ_B , representing the duration between consecutive switches in eigenstates dominated by N_A and N_B , respectively. By collecting sufficiently long traces, we obtain histograms for τ_A (Fig. 2b) and τ_B (Fig. 2c), enabling us to extract characteristic lifetimes T_A and T_B , respectively [13]. Finally, we define $T_{\text{avg}} = (T_A^{-1} + T_B^{-1})^{-1}$ as the average lifetime of the magnetization states. The extracted T_{avg} for atom I–III of the antiferromagnetic Fe_5 chain are shown as a function of the transverse magnetic field in Fig. 2d, showing a pronounced peak at $B_x = 4.1$ T spanning two orders of magnitude. As we will demonstrate below, we can associate this field value to the first DP of the chain $B_{x,1}$. This DP coincides with a minimum in the scattering amplitude, shown by the black solid line in Fig. 2d and defined as $\sum_{a=x,y,z} |\langle \psi_0 | S_{a,i} | \psi_1 \rangle|^2$, which is an indication of the hybridization between ψ_0 and ψ_1 .

Note that the presence of a small longitudinal field induces an avoided level crossing instead of a level crossing, see Supplementary Notes 3 and 6 for further details. This provides the peak in the lifetime with a finite width, enabling us to measure it. The observed trend happens for all atoms of the chain, and is robust to many experimental parameters (see Supplementary Note 4).

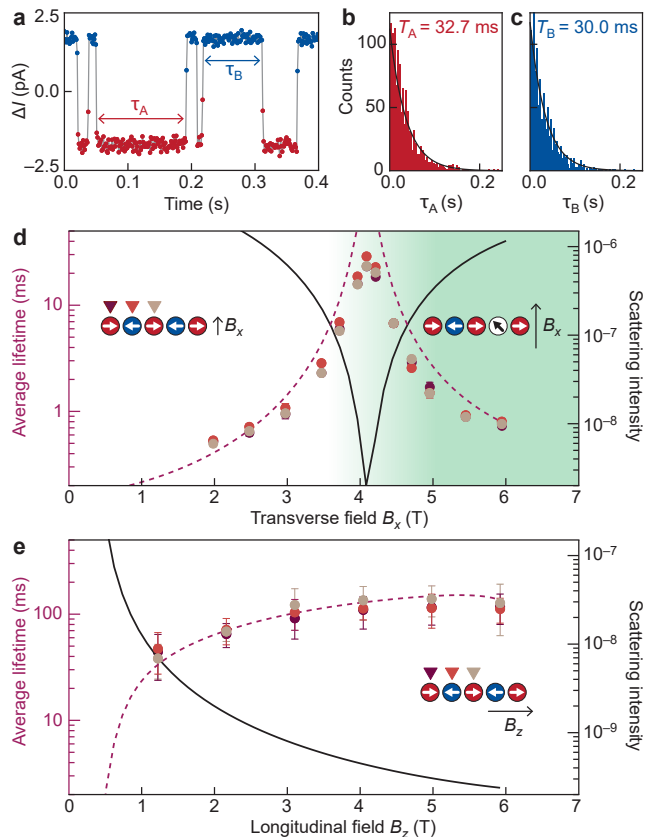


FIG. 2. Lifetime of magnetization states. (a) A current trace obtained at a constant tip height on atom III of the Fe_5 chain near the diabolic point ($B_x = 4$ T). A spin-polarized tip reveals two magnetization states of the chain: N_A (red) and N_B (blue). The data was shifted by about 8 pA to center the middle values around zero, mitigating background fluctuations caused by drift. (b,c) Histograms of lifetimes τ_A and τ_B , as defined in a, with a fit to an exponential function to determine lifetimes T_A and T_B , respectively. (d) Average lifetimes T_{avg} measured for atoms I, II and III of an antiferromagnetic Fe_5 chain at different B_x . The corresponding longitudinal component B_z is approximately 0.35% of the transverse magnetic field, due to a small angle ($\alpha \approx 0.2^\circ$) between the external magnetic field and the crystal axes. Error bars are the standard deviation σ . The lifetime and the scattering intensities calculated using master rate equations are given in the purple dashed and black solid lines, respectively. Background color and diagrams indicate the quanta of S_x in the ground state: zero before the diabolic point and one after the diabolic point, with the diabolic point at $B_{x,1} \approx 4.1$ T. Different colors of data points correspond to measurements performed on different atoms along the chain, see diagram. (e) Lifetime obtained similar to d, but for a magnetic field applied along the longitudinal axis.

The dashed line is a simulation of the lifetime measurements of the chain based on master rate equations (see Supplementary Note 2). Neither the simulations nor the measurements show a peak reaching infinity, owing to minute contributions of states other than N_A and N_B . The experimental data shows slightly lower lifetimes than

the simulation, especially close to the diabolic point. We attribute this deviation to accidental high-energy electrons caused by voltage noise, leading to over-the-barrier excitations.

Until now we have described the situation in terms of the S_z -basis. However, for interpretation purposes, it is insightful to consider the situation in terms of the S_x -basis. For $B_x < 4.1$ T, the expectation value of S_x in the ground state approaches zero, indicated by the white background on the left-side of Fig. 2d and the diagram on the left hand-side. The first excited state contains a single quantum of S_x (i.e. $|\langle S_x \rangle| = 1$). Past the DP, i.e. the avoided level crossing, the states are inverted, transferring the finite S_x magnetization to the ground state, as indicated by the green color of the right-side of Fig. 2d and the diagram on the right hand-side. Note that the ground state now consists of a superposition of five spin states, each having the quantum of S_x on a different atom.

We also demonstrate that the increase of lifetime through the DP emerges only for specific orientation of the magnetic field with respect to the quantization axis. When the magnetic field is swept along the easy axis of the antiferromagnetically coupled Fe_5 chain, no peak in the lifetime is observed, see Fig. 2e. The lifetime slightly increases as a result of decreasing scattering intensity. Within the range of available magnetic fields of B_z (up to ~ 6 T), there is no energy level crossing. Thus, this behaviour is strictly monotonic and results from an increasing imbalance in the Néel state contributions in each eigenstate.

The finite energy difference between the two lowest energy states at the avoided level crossing is responsible for the width of the observed peak in Fig. 2d and therefore limits the efficiency of increasing spin lifetimes. The energy difference at the DP emerges as a consequence of Zeeman energy, resulting from a small angle α between the quantization axis of the Fe atoms with respect to the applied magnetic field. This suggests that in order to achieve a sharper peak, one must achieve a null magnetic field along B_z . This is practically impossible, as α will inevitably be nonzero in our experimental setup. An alternative approach would be to make use of even-length antiferromagnetic chains, where both Néel states have equal energy, irrespective of B_z . In line with this idea, Fig. 3a shows spin lifetimes measured on a Fe_6 chain, where a sharper peak than on the Fe_5 chain is observed.

Despite the expected absence of Zeeman splitting between the two states, the observed peak shows a finite width, which implies that there must be factors breaking the symmetry between the Néel states. Our analysis (see Supplementary Note 5) suggests that the primary cause of the asymmetry is variations in the g -factors of the atoms in the chain. The asymmetry introduced from the tip field has a minor importance. This difference in g -factors results in an energy discrepancy of approximately

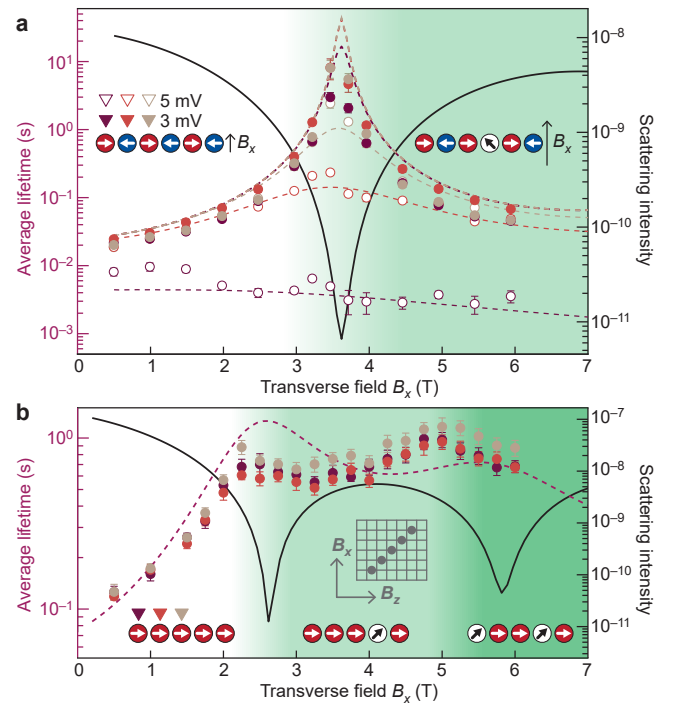


FIG. 3. Tuning diabolic points. (a) Lifetime of an antiferromagnetic Fe_6 chain. Data points given in filled and empty circles were obtained at 3 mV and 5 mV, respectively, for atoms I-III in the chain. Dashed lines are from a simulation of the experiment. Background color and diagram indicate the quanta of S_x in the ground state, which increases from zero to one upon passing the diabolic point. The solid black line indicates the scattering amplitude from the simulation. In this measurement, at 10 pA, 1.3 K, $\alpha \approx 5^\circ$. (b) Similar to panel a, but for a ferromagnetic Fe_5 chain, and $\alpha \approx 0.2^\circ$. Background color and diagrams indicate a second quantum of S_x entering the ground state as the second diabolic point at around 5 T is passed. Note that the easy axis z and hard axis x are defined along the crystallographic directions, see inset. Error bars indicate 2σ .

50 μeV at $B_1 = 6$ T, favoring one Néel state at higher magnetic fields.

The lifetime of the Fe_6 chain increases by nearly three orders of magnitude at the peak, which is shifted to a lower magnetic field compared to Fe_5 . The overall lifetime has also increased, as larger chains are naturally more stable [13]. It is noteworthy that this considerable enhancement of lifetime near the DP is only apparent when the magnetization lifetime is primarily determined by the QTM. Once the over-the-barrier transitions become frequent, the magnetization anomaly diminishes, and we only observe a subtle change in lifetime, as shown in the lifetime curves measured at 5 mV (see also Supplementary Notes 4, 8 and 9). While dehybridization also occurs among higher energy states, as shown in Supplementary Note 2, it appears not to affect the rate of over-the-barrier excitations, for voltages close to the over-the-barrier threshold.

Antiferromagnetic Fe atom chains showed one DP in the transverse magnetic field ranging from 0 T to 6 T. However, adjusting magnetic interactions between atoms in the chain through atom manipulation gives us the possibility to change the location and spacing of DPs. Our simulations indicate that a ferromagnetic Fe₅ chain ($J < 0$) is the most likely candidate where multiple diabolic points can be observed, given the magnetic field range of our experimental setup. In this case, the chain tends to behave as a macrospin with a large total spin. When the coupling is sufficiently strong, this leads to NS positive DPs all equally spaced across the transverse magnetic field. The highest-field DP corresponds to the $B_{x,3}$ value of a single Fe, while the lowest-field DP occurs at $B_{x,3}/(2NS - 1)$. Consequently, the DPs for ferromagnetic chains occur at lower magnetic field values.

We built a ferromagnetic Fe₅ chain by placing the 5 atoms diagonally with respect to the easy axis, see inset of Figure 3b, leading to $J = -0.7$ meV [14]. Figure 3b shows that this chain exhibits two distinct peaks in lifetimes as a function of B_x within our operation range; one at 2.5 T and one at 5.0 T. The second DP is associated with delocalized states where two different atoms in the chain gain a quantum of S_x (i.e. $|\langle S_x \rangle| = 1 \rightarrow 2$). Hence, this may be associated with two-magnon states [20, 21].

The simulation results, see the dashed line in Fig. 3b, qualitatively reproduce the experimental observations but fail to reproduce the exact positions of the DPs. While the scattering intensity does still contain two clearly distinguishable peaks, both the measured and simulated lifetime curves show comparably shallow peaks. We believe that this is due to the overlapping of the two lifetime peaks as well as a larger Zeeman energy associated with the ferromagnetic coupling. The larger energy not only broadens the peaks but also decreases the energy difference between ψ_1 and higher energy states, resulting in more over-the-barrier transitions.

Our work presents a comprehensive approach, combining experimental and theoretical methods, to elucidate the physics of magnetization stability of individual atomic spin chains near a diabolic point. We have demonstrated that the switching rate between the two lowest energy levels can be precisely controlled through tailored transverse magnetic fields, which suppresses quantum tunneling of magnetization. This suppression emerges as a consequence of dehybridization of the lowest lying spin states near an avoided level crossing, which, in the case of Fe chains on Cu₂N, results in strong enhancement of lifetimes up to three orders of magnitude.

While effects of diabolic points have been observed previously in single molecule magnets [2, 8, 9] through ensemble measurements, we showed that diabolic points in quantum magnets can be manipulated and rationally designed by tailoring the interaction of individual atomic spins on surfaces. The composite nature of atomic spin chains provides the possibility to understand the topol-

ogy of diabolic points, with different predicted behaviour for ferromagnetic and antiferromagnetic chains, and a crucial role of parity predicted in the latter case.

The dramatic enhancement of the lifetime provides an interesting avenue into spintronics [17, 22] and applications of coherent spin dynamics [23, 24]. The extreme sensitivity of spin lifetimes of a quantum magnet near a diabolic point could be exploited for precise sensing of local and external magnetic fields at the atomic scale. This sensitivity near diabolic points can also be used to determine parameters of spin Hamiltonians, such a magnetic anisotropy and g-factors, with exquisite precision, leading to further understanding of magnetic material in various applications [25–27].

R.J.G.E., J.C.R. and S.O. acknowledge support from the Netherlands Organisation for Scientific Research (NWO) and from the European Research Council (ERC Starting Grant 676895 “SPINCAD”). D.B., J.O., T.A., J.H., A.J.H., and Y.B. acknowledge support from the Institute for Basic Science (IBS-R027-D1). Y.B. acknowledges support from Asian Office of Aerospace Research and Development (FA2386-20-1-4052). D.B. acknowledges support from the Alexander von Humboldt Foundation for financial support through a Feodor-Lynen Research Fellowship. F.D. acknowledges support from MCIN/AEI/10.13039/501100011033, and “FEDER, a way to make Europe”, by the European Union (PID2022-138269NB-I00).

All simulations, raw data, code to process the data, figures and data points on the figures in the main text and the Supplementary Information [28] are available from the Open Data folder accessible through the digital object identifier (“DOI”) 10.5281/zenodo.10906000.

The authors declare no competing interests.

*Corresponding authors: F.D. (fdelgado@ull.edu.es), S.O. (a.f.otte@tudelft.nl), Y.B. (bae.yujeong@qns.science)

-
- [1] M. V. Berry and M. Wilkinson, *Diabolical points in the spectra of triangles*, *Proc. R. Soc. London A: Math. Phys. Eng. Sci.*, vol. 392, no. 1802, pp. 15–43, 1984. doi: 10.1098/rspa.1984.0022
 - [2] W. Wernsdorfer and R. Sessoli, *Quantum Phase Interference and Parity Effects in Magnetic Molecular Clusters*, *Science*, vol. 284, no. 5411, pp. 133–135, 1999. doi: 10.1126/science.284.5411.133
 - [3] R. Sessoli, D. Gatteschi, A. Caneschi, and M. A. Novak, *Magnetic bistability in a metal-ion cluster*, *Nature*, vol. 365, no. 6442, pp. 141–143, 1993. doi:10.1038/365141a0
 - [4] L. Thomas, F. Lioni, R. Ballou, D. Gatteschi, R. Sessoli, and B. Barbara, *Macroscopic quantum tunnelling of mag-*

- netization in a single crystal of nanomagnets, *Nature*, vol. 383, no. 6596, pp. 145–147, 1996. doi:10.1038/383145a0
- [5] J. von Delft and C. L. Henley, *Destructive quantum interference in spin tunneling problems*, *Phys. Rev. Lett.*, vol. 69, no. 22, pp. 3236–3239, Nov 1992. doi:10.1103/PhysRevLett.69.3236
- [6] D. Loss, D. P. DiVincenzo, and G. Grinstein, *Suppression of tunneling by interference in half-integer-spin particles*, *Phys. Rev. Lett.*, vol. 69, no. 22, pp. 3232–3235, Nov 1992. doi:10.1103/PhysRevLett.69.3232
- [7] A. Garg, *Topologically Quenched Tunnel Splitting in Spin Systems without Kramers’ Degeneracy*, *Europhysics Letters*, vol. 22, no. 3, p. 205, Apr 1993. doi:10.1209/0295-5075/22/3/008
- [8] E. Burzurí, F. Luis, O. Montero, B. Barbara, R. Ballou, and S. Maegawa, *Quantum Interference Oscillations of the Superparamagnetic Blocking in an Fe₈ Molecular Nanomagnet*, *Phys. Rev. Lett.*, vol. 111, no. 5, p. 057201, Jul 2013. doi:10.1103/PhysRevLett.111.057201
- [9] W. Wernsdorfer, N. E. Chakov, and G. Christou, *Quantum Phase Interference and Spin-Parity in Mn₁₂ Single-Molecule Magnets*, *Phys. Rev. Lett.*, vol. 95, no. 3, p. 037203, Jul 2005. doi:10.1103/PhysRevLett.95.037203
- [10] C. F. Hirjibehedin, C.-Y. Lin, A. F. Otte, M. Ternes, C. P. Lutz, B. A. Jones, and A. J. Heinrich, *Large Magnetic Anisotropy of a Single Atomic Spin Embedded in a Surface Molecular Network*, *Science*, vol. 317, no. 5842, pp. 1199–1203, 2007. doi:10.1126/science.1146110
- [11] F. D. Natterer, F. Donati, F. Patthey, and H. Brune, *Thermal and Magnetic-Field Stability of Holmium Single-Atom Magnets*, *Phys. Rev. Lett.*, vol. 121, no. 2, p. 027201, Jul 2018. doi:10.1103/PhysRevLett.121.027201
- [12] A. Singha, P. Willke, T. Bilgeri, X. Zhang, H. Brune, F. Donati, A. J. Heinrich, and T. Choi, *Engineering atomic-scale magnetic fields by dysprosium single atom magnets*, *Nature Communications*, vol. 12, no. 1, p. 4179, 2021. doi:10.1038/s41467-021-24465-2
- [13] S. Loth, S. Baumann, C. P. Lutz, D. M. Eigler, and A. J. Heinrich, *Bistability in Atomic-Scale Antiferromagnets*, *Science*, vol. 335, no. 6065, pp. 196–199, 2012. doi:10.1126/science.1214131
- [14] A. Spinelli, B. Bryant, F. Delgado, J. Fernández-Rossier, and A. F. Otte, *Imaging of spin waves in atomically designed nanomagnets*, *Nature Materials*, vol. 13, p. 782, Jul 2014. doi:10.1038/nmat4018
- [15] Cyrus F. Hirjibehedin, Christopher P. Lutz, Andreas J. Heinrich, *Spin Coupling in Engineered Atomic Structures*, *Science*, **312**(5776), 1021–1024 (2006), doi:10.1126/science.1125398.
- [16] Shichao Yan, Deung-Jang Choi, Jacob A. J. Burgess, Steffen Rolf-Pissarczyk, Sebastian Loth, *Control of quantum magnets by atomic exchange bias*, *Nature Nanotechnology*, **10**, 40 (2014), doi:10.1038/nnano.2014.281.
- [17] R. J. G. Elbertse, D. Coffey, J. Gobeil, A. F. Otte, *Remote detection and recording of atomic-scale spin dynamics*, *Communications Physics*, **3**(1), 94 (2020), doi:10.1038/s42005-020-0361-z.
- [18] Patrick Bruno, *Berry Phase, Topology, and Degeneracies in Quantum Nanomagnets*, *Phys. Rev. Lett.*, **96**(11), 117208 (2006), doi:10.1103/PhysRevLett.96.117208.
- [19] R. Žitko, Th Pruschke, *Many-particle effects in adsorbed magnetic atoms with easy-axis anisotropy: the case of Fe on the CuN/Cu(100) surface*, *New Journal of Physics*, **12**(6), 063040 (2010), doi:10.1088/1367-2630/12/6/063040.
- [20] H. Bethe, *Zur Theorie der Metalle*, *Zeitschrift für Physik*, **71**(3), 205–226 (1931), doi:10.1007/BF01341708.
- [21] F. Delgado, M. M. Otrokov, A. Arnau, *Spin wave excitations in low dimensional systems with large magnetic anisotropy*, arXiv preprint, [arXiv:2310.15942](https://arxiv.org/abs/2310.15942) (2023), doi:10.48550/arXiv.2310.15942.
- [22] Wolfgang Wernsdorfer, *Molecular nanomagnets: towards molecular spintronics*, *International Journal of Nanotechnology*, **7**(4-8), 497–522 (2010), doi:10.1504/IJNT.2010.031732.
- [23] Susanne Baumann, William Paul, Taeyoung Choi, Christopher P. Lutz, Arzhang Ardavan, Andreas J. Heinrich, *Electron paramagnetic resonance of individual atoms on a surface*, *Science*, **350**(6259), 417–420 (2015), doi:10.1126/science.aac8703.
- [24] Kai Yang, William Paul, Soo-Hyon Phark, Philip Willke, Yujeong Bae, Taeyoung Choi, Taner Esat, Arzhang Ardavan, Andreas J. Heinrich, Christopher P. Lutz, *Coherent spin manipulation of individual atoms on a surface*, *Science*, **366**(6464), 509–512 (2019), doi:10.1126/science.aay6779.
- [25] Lourdes Marcano et al., *Magnetic Anisotropy of Individual Nanomagnets Embedded in Biological Systems Determined by Axi-asymmetric X-ray Transmission Microscopy*, *ACS Nano*, **16**(5), 7398–7408 (2022), doi:10.1021/acsnano.1c09559.
- [26] Q A Pankhurst, J Connolly, S K Jones, J Dobson, *Applications of magnetic nanoparticles in biomedicine*, *Journal of Physics D: Applied Physics*, **36**(13), R167 (2003), doi:10.1088/0022-3727/36/13/201.
- [27] Wolfgang Wernsdorfer, N. E. Chakov, G. Christou, *Determination of the magnetic anisotropy axes of single-molecule magnets*, *Phys. Rev. B*, **70**(13), 132413 (2004), doi:10.1103/PhysRevB.70.132413.
- [28] Supplemental Material, *See Supplemental Material at [URL-will-be-inserted-by-publisher] for an overview of experimental parameters, for additional simulations and for additional control experiments.*
- [29] J. Fernández-Rossier, *Theory of Single-Spin Inelastic Tunneling Spectroscopy*, *Phys. Rev. Lett.* **102**, 256802 (2009), doi:10.1103/PhysRevLett.102.256802.
- [30] F. Delgado, J. J. Palacios, and J. Fernández-Rossier, *Spin-Transfer Torque on a Single Magnetic Adatom*, *Phys. Rev. Lett.* **104**, 026601 (2010), doi:10.1103/PhysRevLett.104.026601.
- [31] S. Loth, M. Etzkorn, C. P. Lutz, D. M. Eigler, and A. J. Heinrich, *Measurement of Fast Electron Spin Relaxation Times with Atomic Resolution*, *Science* **329**, 1628–1630 (2010), doi:10.1126/science.1191688.
- [32] S. Loth, C. P. Lutz, and A. J. Heinrich, *Spin-polarized spin excitation spectroscopy*, *New Journal of Physics* **12**, 125021 (2010), doi:10.1088/1367-2630/12/12/125021.
- [33] J. W. Nicklas, A. Waddehra, and J. W. Wilkins, *Magnetic properties of Fe chains on Cu₂N/Cu(100): A density functional theory study*, *Journal of Applied Physics* **110**, 123915 (2011), doi:10.1063/1.3672444.
- [34] B. Bryant, A. Spinelli, J. J. T. Wagenaar, M. Gerrits, and A. F. Otte, *Local Control of Single Atom Magnetocrystalline Anisotropy*, *Phys. Rev. Lett.* **111**, 127203 (2013), doi:10.1103/PhysRevLett.111.127203.
- [35] S. Yan, D.-J. Choi, J. A. J. Burgess, S. Loth, *Three-Dimensional Mapping of Single-Atom Magnetic Anisotropy*, *Nano Letters* **15**, 1938–1942 (2015), doi:

- 10.1021/nl504779p.
- [36] S. Yan, L. Malavolti, J. A. J. Burgess, A. Droghetti, A. Rubio, S. Loth, *Nonlocally sensing the magnetic states of nanoscale antiferromagnets with an atomic spin sensor*, *Science Advances* **3**, e1603137 (2017), doi:10.1126/sciadv.1603137.
- [37] S. Rolf-Pissarczyk, S. Yan, L. Malavolti, J. A. J. Burgess, G. McMurtrie, S. Loth, *Dynamical Negative Differential Resistance in Antiferromagnetically Coupled Few-Atom Spin Chains*, *Phys. Rev. Lett.* **119**, 217201 (2017), doi:10.1103/PhysRevLett.119.217201.
- [38] C. Rudowicz, K. Tadyszak, T. Ślusarski, Marcos Verissimo-Alves, and M. Kozanecki, *Modeling Spin Hamiltonian Parameters for Fe²⁺ (*S*=2) Adatoms on Cu₂N/Cu(100) Surface Using Semiempirical and Density Functional Theory Approaches*, *Applied Magnetic Resonance* **50**(6), 769-783 (2019), doi:10.1007/s00723-018-1059-1.
- [39] S. Loth, K. von Bergmann, M. Ternes, A. F. Otte, C. P. Lutz, and A. J. Heinrich, *Controlling the state of quantum spins with electric currents*, *Nature Physics* **6**(5), 340-344 (2010), doi:10.1038/nphys1616.
- [40] F. Delgado and J. Fernández-Rossier, *Spin decoherence of magnetic atoms on surfaces*, *Progress in Surface Science* **92**(1), 40-82 (2017), doi:10.1016/j.progsurf.2016.12.001.
- [41] J. Hwang *et al.*, *Development of a scanning tunneling microscope for variable temperature electron spin resonance*, *Review of Scientific Instruments* **93**(9), 093703 (2022), doi:10.1063/5.0096081.
- [42] W. Paul, K. Yang, S. Baumann, N. Romming, T. Choi, C. P. Lutz, and A. J. Heinrich, *Control of the millisecond spin lifetime of an electrically probed atom*, *Nature Physics* **13**(4), 403-407 (2017), doi:10.1038/nphys3965.
- [43] M. Yamada, K. Nakatsuji, and F. Komori, *Nitrogen Adsorption on Cu(001): Mechanisms of Stress Relief and Coexistence of Two Domains*, *e-Journal of Surface Science and Nanotechnology* **21**(4), 337-343 (2023), doi:10.1380/ejsnt.2023-044.

SUPPLEMENTARY NOTE 1: PARAMETERS USED IN THE SIMULATIONS

In the Hamiltonian given in the main text (Eq. 1), the parameters (D_i , E_i , g_i , and J_{ij}) specified for Fe on Cu₂N have been experimentally investigated. The values found in the literature are summarized in Table I, showing significant variations among adatoms. These discrepancies can be attributed to variations of local environments influenced by factors such as strains in the underlying Cu₂N layer, nearby defects, and adjacent atoms. While previous studies derived parameters from bias spectroscopy, our approach involved extracting values only based on lifetime curves, but referred to the literature values in Table I to facilitate optimizing the parameters for simulations. The simulations are based on the Master Rate Equations [29–31].

N	D (meV)	E (meV)	J (meV)	g	Source	Year
1	-1.55 ± 0.01	0.31 ± 0.01		2.11 ± 0.05	[10]	2007
1	-1.55 ± 0.02	0.31 ± 0.01		2.11	[32]	2010
3 (sim.)	-1.53	0.37	> 25		[33]	2011
≥ 3			1.3 ± 0.1		[13]	2012
2	-1.87	0.31	0.7		[34]	2013
2 (FM)	-1.37	0.31	-0.69		[34]	2013
6 (FM)	-1.29	0.31	-0.73		[14]	2014
1	-1.59 ± 0.03	0.31 ± 0.01		2.07 ± 0.19	[35]	2015
3	$\{-2.1, -3.6, -2.1\}$	0.31	1.15 ± 0.1	2.1	[16]	2015
3	$\{-2.1, -3.6, -2.1\}$	0.3	1.15	2	[36]	2017
3	$\{-1.88, -2.42, -1.87\}$	$\{0.39, 0.2, 0.31\}$	$\{0.71, 0.66\}$		[37]	2017
1 (sim.)	-1.53	< 0		2.14 ± 0.12	[38]	2019
3, 5	-1.87	0.31	0.7	2.11	[17]	2020

TABLE I. **Overview of literature values for parameters in the Hamiltonian.** The first column shows the number of atoms N . The values given in the table are mostly obtained from experiments conducted on antiferromagnetically coupled Fe atomic chains, except for instances labeled as "(sim.)" and "(FM)", denoting studies based on simulation results and ferromagnetic chains, respectively. The second column describes the uniaxial magnetic anisotropy term D , either considered equal for all atoms or uniquely defined for each atom (three cases of trimers). The third column describes the transverse magnetic anisotropy parameter E and has one study with a unique definition for each individual atom of a trimer. Ref. [38] found this to be negative, contrary to our definition. The fourth column describes the Heisenberg exchange coupling strength J , showing both ferromagnetic ($J < 0$) and antiferromagnetic ($J > 0$) couplings. A study [33] reporting J larger than 25 meV is inconsistent with our observations. Ref. [37] describes different coupling strengths between different neighbours in a trimer. The fifth column describes the g -factor. The sixth and seventh columns provide the reference and publication year of these studies, respectively.

Table II provides a summary of the parameters used in the simulations of each figure. The simulation result used for Fig. 1a was processed by subtracting a linear slope along B_x for clear visualization of the diabolic point. In the other simulations, we

Parameter	Figure 1a	Figure 2d	Figure 2e	Figure 3a	Figure 3b
N	1	5	5	6	5
D (meV)	-1.87	$\{-2.05, -2.35, -2.85, \dots\}$	$\{-2.1, -2.3, -2.85, \dots\}$	$\{-1.95, -2.25, -2.80, \dots\}$	-1.70 (all)
E (meV)	0.31	$\{0.33, 0.32, 0.32, \dots\}$	0.32 (all)	0.3 (all)	0.4 (all)
J (meV)		$\{0.85, 1, \dots\}$	0.83 (all)	$\{0.85, 0.95, 1.35, \dots\}$	-0.95 (all)
g	2.11	$\{2.5, 2.11, 2.11, 2.11\}$	$\{2.5, 1.9, 2.5, 1.9, 1.8\}$	$\{2.4, 2.11, 2.11, 2.11, 2.11, 2.11\}$	$\{2.5, 2.11, 2.11, 2.11, 2.11\}$
B_{tip} (mT)		50 on atom i	100 on atom i	-110 on probed atom	-60 on atom i
α ($^\circ$)		0.2	0.8	4.1	0.2
T (K)		3	1.3	2.3	1.3
V (mV)		3	3	2.75 (purple), 4.75 (grey)	3
G_{SS} (μS)		1	4	4	4
η		0.5	0.5	0	0.5

TABLE II. **Overview of parameters used in the simulations presented in the main text.** D , E , J , and g are the same parameters as given in Table 1. B_{tip} represents the magnetic field induced on a single atom due to the tip field along B_z , α the angle between the external magnetic field and the crystal lattice, V the voltage applied for measurements, G_{SS} the electron coupling with the bath, and η the polarization of the tip. For D , E , J , and g , a list of values is given, corresponding to the values on or between the various atoms, starting with atom I. Here an ellipsis (“...”) indicates that the remaining values are symmetric with respect to the previous values (following a, b, c, b, a for $N = 5$, and a, b, c, c, b, a for $N = 6$).

considered angles, α and β , representing the directions of the applied magnetic field with respect to the crystal axes (further details in Supplementary Note 3). In addition to the external magnetic field, the tip magnetic field induced by the magnetic interaction between the magnetic tip and the atom beneath it was considered. Note that we considered the B_z component only, given the negligibly small tip field along B_x compared to the external field. The coupling with the substrate is given as $G_{\text{SS}} = 1 \mu\text{S}$, following the definition given in [37].

Noting that the simulation shows lifetimes larger than the experimental values, especially closer to the peak center, we believe the measured lifetime is limited by accidental voltage spikes that may cause over-the-barrier transitions. This is corroborated by longer lifetimes measured upon better grounding of thermometry lines close to the current line. While we did not find a proper way to include such spurious voltages in the model, the simulations were performed with elevated temperatures to account for the on-average higher electron energy. We believe there has been a small voltage offset during the measurements of Fig. 3a, resulting in voltages slightly below the intended values. For Fig. 2 and 3b, we introduced a relatively strong tip polarization η (defined between -1 and $+1$), which gives better match between the simulation and experimental results. To expedite the processing time, only the lowest 250 energy eigenstates were considered, with only the 500 largest contributions of spin eigenstates within these energy eigenstates.

SUPPLEMENTARY NOTE 2: SIMULATIONS OF LIFETIME AROUND A DIABOLIC POINT

The simulations to describe the evolution of lifetime as a function of the external magnetic fields are based on rate equations [29, 30, 39], which include transitions between various states following spin-selection and energy conservation rules. These transitions can be derived by including the exchange coupling of the local spins with the itinerant electrons [40]. In a semiclassical description, under an applied longitudinal field B_z , a spin S with an easy-axis anisotropy exhibits the ground state ψ_0 with $m_s = -S$ along the easy axis and the first excited state ψ_1 with $m_s = +S$. Thus transitions between these states while exchanging spin angular momentum with tunneling electrons necessitate passing through intermediate states, adhering to the spin conservation rule ($\Delta m_s = \pm 1$). These intermediate states are higher in energy, which requires tunneling electrons with sufficient energy to overcome the effective energy barrier. In a quantum mechanical framework, states ψ_0 and ψ_1 experience slight hybridization, leading to direct transitions between them without exchanging the spin angular momentum ($\Delta m_s = 0$). For a single Fe atom on Cu_2N , the transverse magnetic anisotropy induces this hybridization, resulting in the ground state comprising a linear combination of spin states $m_s = -2$ and $m_s = +2$. This hybridization facilitates Quantum Tunneling of Magnetization (QTM), leading to direct transitions between both states.

We can thus differentiate between two types of transitions. First, there is the so-called flip-flop transition where the magnetic angular momentum of the tunneling electron is exchanged with the one of the atom, leading to $\Delta m_s = \pm 1$, which is the primary cause of over-the-barrier transitions and is expressed as $\langle \psi_0 | S_{\pm, i} | \psi_1 \rangle$. Secondly, there is a so-called direct transition, where $\Delta m_s = 0$, which is the primary cause of QTM. By suppressing the hybridization, the direct transitions, whose intensities depend on $\langle \psi_0 | S_{z, i} | \psi_1 \rangle$, are suppressed. This quenching reduces the switching rates due to QTM, consequently leading to longer lifetimes in the absence of over-the-barrier excitations. The transition likelihood between ψ_0 and ψ_1 for a single tunneling electron can be encapsulated by the scattering intensity $P_{0,1} = \sum_{a=x,y,z} |\langle \psi_0 | S_{a, i} | \psi_1 \rangle|^2$, which is plotted in Figs. 2d, 2e, 3a and 3b and is a measure for how likely QTM is.

More specifically, in the absence of an external magnetic field, hybridization occurs from the transverse magnetic anisotropy term $E(S_x^2 - S_y^2) = E(S_+^2 + S_-^2)/2$. For a single Fe atom with $S = 2$, the magnetic anisotropy terms, $D = -1.87$ meV and $E = 0.31$ meV, result in the ground state of $\psi_0 = (0.7, 0, -0.139, 0, 0.7)$ as a symmetric superposition of $m_s = \pm 2$. The first excited state $\psi_1 = (0.707, 0, 0, 0, -0.707)$ represents an antisymmetric superposition. Figure 4a and b show how these states evolve when sweeping B_x as given by the S_z and S_x basis, respectively.

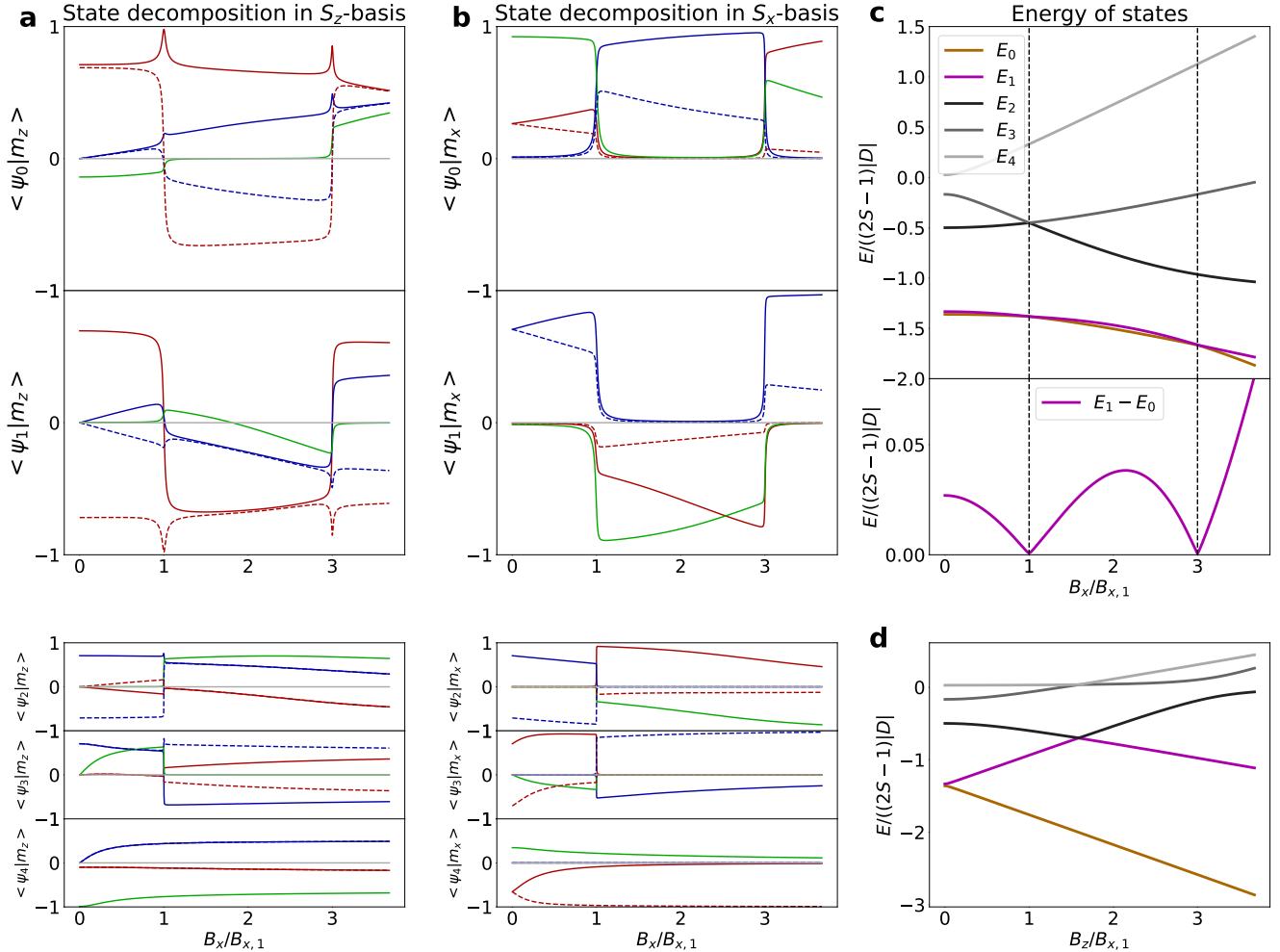


FIG. 4. **State decomposition of the single Fe atom as a function of B_x .** (a) Decomposition of ψ_0 and ψ_1 (top) in the S_z -basis, and ψ_2 through ψ_4 (bottom) as a function of B_x divided by $B_{x,1}$, the field value of the first diabolic point. (b) Same but in the S_x -basis. Red curves represent $m_s = \pm 2$, blue curves correspond to $m_s = \pm 1$, and a green curve is for $m_s = 0$ in the respective basis. Dashed lines are for $m_s > 0$. (c) (top) Energies of the five states of the single Fe atom over the same magnetic field range as panels a and b. The abrupt changes in the decomposition curves around $B_{x,1}$ and $3B_{x,1}$ correspond to avoided level crossings in the energy spectrum. (bottom) Energy difference between ψ_0 and ψ_1 from the top panel. (d) Energies of the five states when the magnetic field is applied along B_z instead. In all cases, there is 10 mT in the other in-plane direction to induce smooth avoided level crossings.

Around $B_{x,1}$ and $3B_{x,1} = B_{x,3}$, there are avoided level crossings between ψ_0 and ψ_1 (Fig. 4c), where the two states effectively swap their spin composition. In terms of S_z -basis, this results in a switching of the symmetry, i.e., for the first avoided level crossing, a transition from $|\psi_0\rangle \sim (|-2\rangle_z + |+2\rangle_z)/\sqrt{2}$ to $|\psi_0\rangle \sim (|-2\rangle_z - |+2\rangle_z)/\sqrt{2}$. In the process, the $\langle \psi_0 | +2\rangle_z$ contribution goes through zero while the $\langle \psi_0 | -2\rangle_z$ one increases in contribution. A similar effect happens at the second avoided level crossing. In both cases, at the exact crossing points, ψ_0 has zero contribution of $m_z = +2$ and ψ_1 has zero contribution of $m_z = -2$. This significantly suppresses the $\Delta m_z = 0$ transition probability between the two states, compared to field values far from these crossings. The width of the lifetime peak vs. B_x , or, alternatively, the width of the avoided level crossing in the energy spectrum (see Fig. 4c) is ultimately determined by the B_z -field, being strictly zero when $B_z = 0$. For

a finite B_z , the hybridization between the $|\pm 2\rangle_z$ states is reduced, and the quenching of the QTM near a DP survives in a larger B_x -window. This quenching also happens between ψ_2 and ψ_3 , although the effect is much sharper as the B_x field has a much more drastic effect on the energy splitting between the ψ_2 and ψ_3 states.

While the S_z -basis is convenient for explaining the critical behaviour of lifetimes near the diabolic point, a better insight into the underlying mechanism can be gained using the basis of spin states along the applied field, i.e., the S_x -basis (Fig. 4b). For small B_x , ψ_0 is dominated by $m_x = 0$ with minor contribution in $m_x = \pm 2$ due to the transverse magnetic anisotropy. At the first diabolic point, ψ_0 and ψ_1 swap their spin compositions. Thus, ψ_0 converts from a state dominated by $m_x = 0$ to one dominated by $m_x = -1$. Then, at the second diabolic point, ψ_0 converts into a state dominated by $m_x = -2$. Hence, at each diabolic point, a quantum of S_x enters the ground state. As shown in Fig. 4, abrupt changes in both energy spectra and states' composition only appears near the DPs.

In summary, we can understand each crossing between ψ_0 and ψ_1 as the change of a quantum of S_x in the ground state. Thus, as B_x is swept, the ground state changes from the majority state of $m_x = 0$ to $m_x = -1$ after the first crossing and to $m_x = -2$ after the second crossing. In terms of the S_z state composition, an additional unit of S_x results in alternating symmetry in the linear combinations of $m_z = \pm m$ for any m . This swapping of symmetry results in values of B_x where the hybridization is minimized, ultimately leading to maxima in the lifetimes.

Compared to the single Fe atom, the behaviour of spin chains is more intricate but fundamentally based on the same physics for weak coupling between the atoms. The number of diabolic points grows with the total spin of the system and, consequently, with the number of atoms N . This is illustrated in Fig. 5 where, using the same values of D , E , and g , we calculated all positive diabolical points $B_x^{N,j}$ for the $j \in \{1, \dots, NS\}$ values of chains with $N = 2 - 6$ spins for different coupling strengths of J including both ferromagnetic ($J < 0$, Fig. 5a) and antiferromagnetic ($J > 0$, Fig. 5b) cases. The $N = 5$ case is shown in thick black lines for clarity. The value $j = 1$ corresponds to the lowest DP. In Fig. 5c, we narrow our focus to a smaller window aligned with experimental conditions.

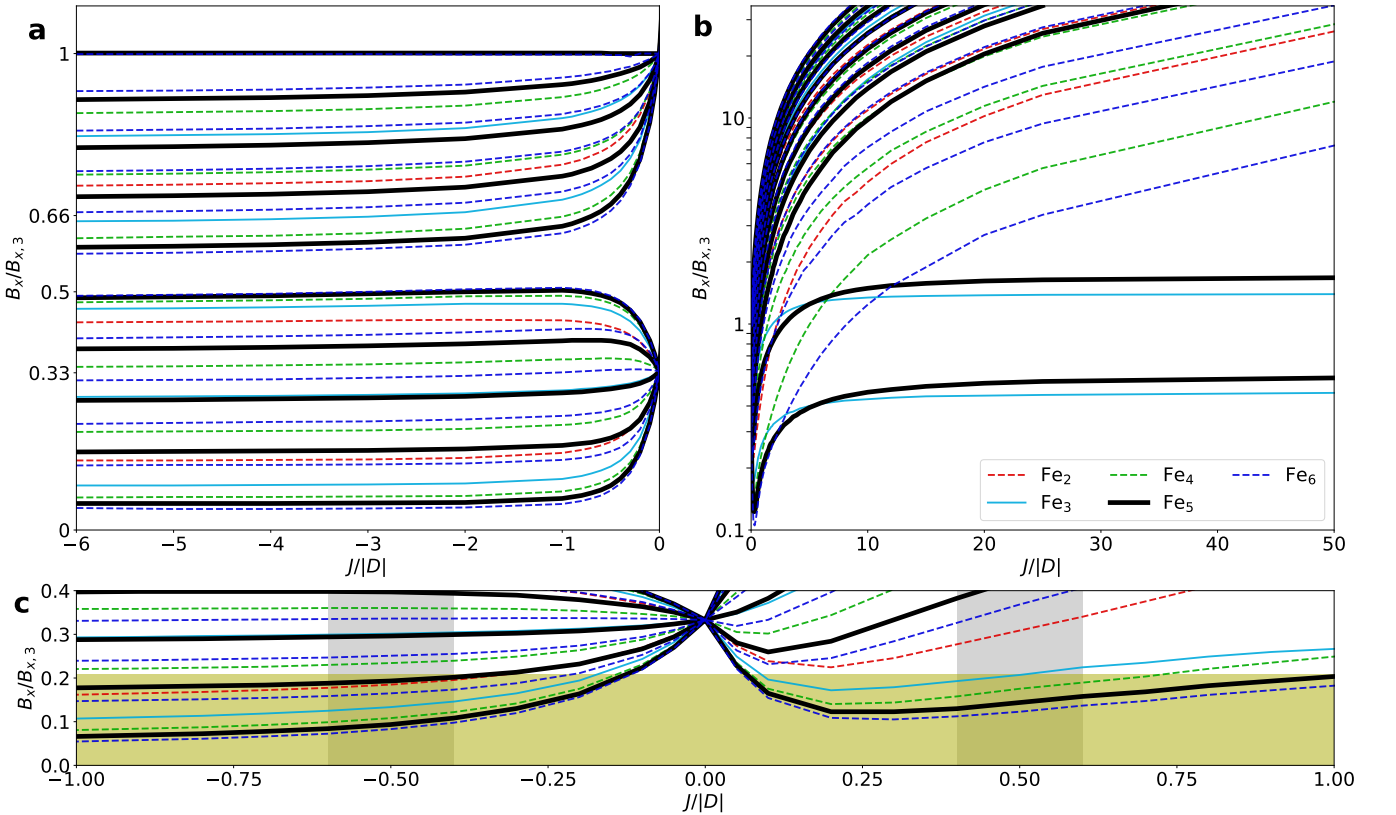


FIG. 5. Magnetic field values of diabolic points for Fe chains with different lengths $N = \{2, 3, 4, 5, 6\}$ and different coupling strengths $J/|D|$. (a) Ferromagnetically coupled atomic chains ($J/|D| \leq 0$) in a linear scale. (b) Antiferromagnetically coupled case ($J/|D| > 0$) in a logarithmic scale to facilitate comparison under different regimes. (c) Zoom-in for $|J/|D| \leq 1$ and $B_x \leq 0.4B_{x,3}$. The shaded region contains values of B_x and $J/|D|$ relevant to the experiments performed throughout this work. The horizontal shaded region indicates our external magnetic field range. All plots were constructed by finding degeneracies between ψ_0 and ψ_1 as a function of B_x (here, $B_z = 0$). The legend presented in panel b applies to all panels. To facilitate comparison, solid lines (dashed lines) indicate odd (even) number chains.

For $J = 0$, the N atoms are decoupled, resulting in the same diabolic points at $B_{x,1}$ and $B_{x,3}$. As $|J|$ increases, the degeneracy between atoms is lifted, leading to the dispersion of diabolic points into multiple branches. The number of these branches corresponds to the number of atoms in the chain. Consequently, by increasing j , the quanta of S_x in the ground state increase upon passing the j^{th} -DP, as happened twice for Fig. 3b.

There is a major difference between the ferromagnetic and antiferromagnetic chains. The ferromagnetic case (Fig. 5a) is certainly more intuitive: as $-J/|D|$ increases, the diabolic points tend towards the DPs of a macrospin of dimension NS . This can be observed in the spacing between each subsequent diabolic point, which follows the same spacing as described in Eq. 2 of the main text. Surprisingly, irrespective of the length of the chain, the highest diabolic point is always equal to $B_{x,3}$. This implies that the lowest diabolic point can be found at $B_{x,3}/(2SN - 1)$, and the next diabolic point can be found at three times this value. The ferromagnetic chain in the main text has a ratio $B_x^{5,2}/B_x^{5,1} \sim 2$, suggesting that $|J|$ is too small to consider the chain as a single macrospin, consistent with our simulations.

For the antiferromagnetic ($J > 0$) chain (Fig. 5b), when $J/|D| \gg 1$, the odd-numbered chains present S DPs at $B_x \lesssim B_{x,2S-1}$. This corresponds to the uncompensated spin in such chains. This may also open the possibility of exploring diabolic points in Mn_N -chains as the ones explored by Hirjibehedin *et al.* [15], where $J/|D| \approx 160$ [10] and $B_{x,1} \approx 0.5$ T. Simulations show lifetime peaks at around 0.75 T and 1.5 T for Mn_3 and at around 1 T and 2 T for Mn_5 .

In agreement with our experimental observations, Fig. 5c shows that as N increases for values $|J/|D| \approx 0.5$, the lowest diabolic point $B_{x,1}^{N,1}$ is found at smaller values of B_x . For much larger J , all DPs of even-numbered antiferromagnetic chains diverge to extreme values. It also shows that in our operable window (up to about $0.21B_{x,3}$), the easiest way to measure multiple DPs is by going to ferromagnetic chains. We had considered antiferromagnetic chains of longer length, like Fe_8 . However, the time needed to measure statistically relevant data at the DP exceeded the scope of this work.

The only noteworthy effect of local changes in the g -factors is a small splitting of the $B_x^{N,j}$ diabolic points when $|J/D| \rightarrow 0$, not shown in the figure.

SUPPLEMENTARY NOTE 3: SAMPLE ORIENTATION

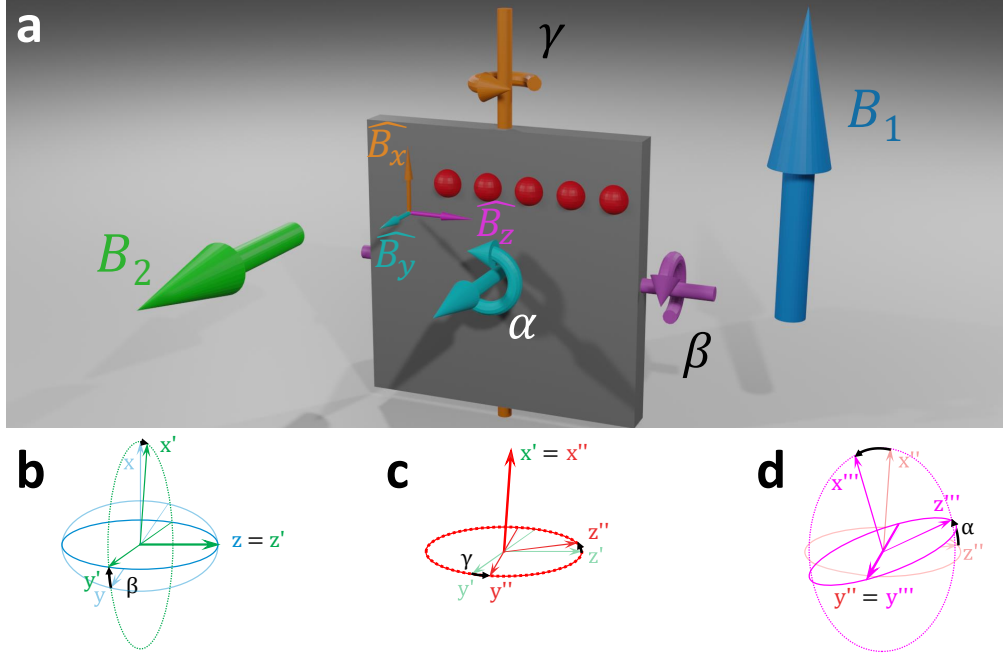


FIG. 6. **Alignments of the sample with magnetic fields.** (a) The substrate is given as a square plate, on which five red spheres represent the Fe_5 atom chain. The substrate's orientation can be adjusted along three axes through angles α , β , and γ . An external magnetic field, facilitated by a two-axis vector magnet, can be applied along \mathbf{B}_1 and \mathbf{B}_2 . Due to misalignment between the crystal axes and the magnetic field directions, the applied fields can be decomposed into B_x , B_y and B_z for the chains in terms of crystal axes. (b) Tait-Bryan rotation along the z -axis with an angle β . A negative value of β is shown to represent the actual angle $\sim -8^\circ$. (c) Tait-Bryan rotation along the x' -axis with an angle γ . A small value γ is shown to represent the near negligible actual value. (d) Tait-Bryan rotation along the y'' -axis with an angle α . A large value of α is shown to represent the actual large variability of α in the work presented here.

Since the shape of the lifetime curves strongly depends on the exact orientation and magnitude of the applied magnetic field, particularly the B_z component, the precise characterization of magnetic field components with respect to the crystal axes is crucial. Figure 6 shows the Fe_5 chain on a $\text{Cu}(100)$ crystal, illustrating the directions of the external magnetic field and the crystal axes. In our experiment, we found that the crystal axes are not fully aligned with the external magnetic field directions due to several reasons:

1. The sample holder, designed for a certain angle ($\sim 8^\circ$) for the cold deposition [41], contributes significantly to the misalignment between \mathbf{B}_1 and \mathbf{B}_x , resulting in the angle $\beta \approx -8^\circ$.
2. Mounting the $\text{Cu}(100)$ crystal to the sample holder introduces a slight in-plane rotation, which gives a finite α . This can be estimated from the atomic resolution images and adjusted by remounting the crystal (Fig. 9b,d,f).
3. There is a subtle misalignment between the STM stage and the magnetic field axes, which affects all three angles. From the experiment, we found the effects on γ and β are negligibly small while giving $\sim 3^\circ$ deviation for α , denoted as α_{tilt} .

The resulting combination of rotations can be expressed in a sequence of Tait-Bryan rotations, as indicated in Fig. 6b-d. Applying the rotations in the given order results in the following decomposition of the external field:

$$\begin{aligned}
 B_x &= B_1(\cos \alpha \cos \beta - \sin \alpha \sin \beta \sin \gamma) + B_2(\cos \alpha \sin \beta + \sin \alpha \cos \beta \sin \gamma) \\
 B_y &= B_1(-\sin \beta \cos \gamma) + B_2(\cos \beta \cos \gamma) \\
 B_z &= B_1(\sin \alpha \cos \beta + \cos \alpha \sin \beta \sin \gamma) + B_2(\sin \alpha \sin \beta - \cos \alpha \cos \beta \sin \gamma)
 \end{aligned} \tag{3}$$

In the limit where $\gamma = 0$, $B_2 = 0$, $|\beta| \ll \pi/2$ and $|\alpha| \ll \pi/2$, these equations can be simplified to:

$$\begin{aligned}
B_x &= B_1(\cos \alpha \cos \beta) \\
B_y &= B_1(-\sin \beta) \\
B_z &= B_1(\sin \alpha \cos \beta)
\end{aligned}
\tag{4}$$

SUPPLEMENTARY NOTE 4: VARIATION OF LIFETIME CURVES AT DIFFERENT CONDITIONS

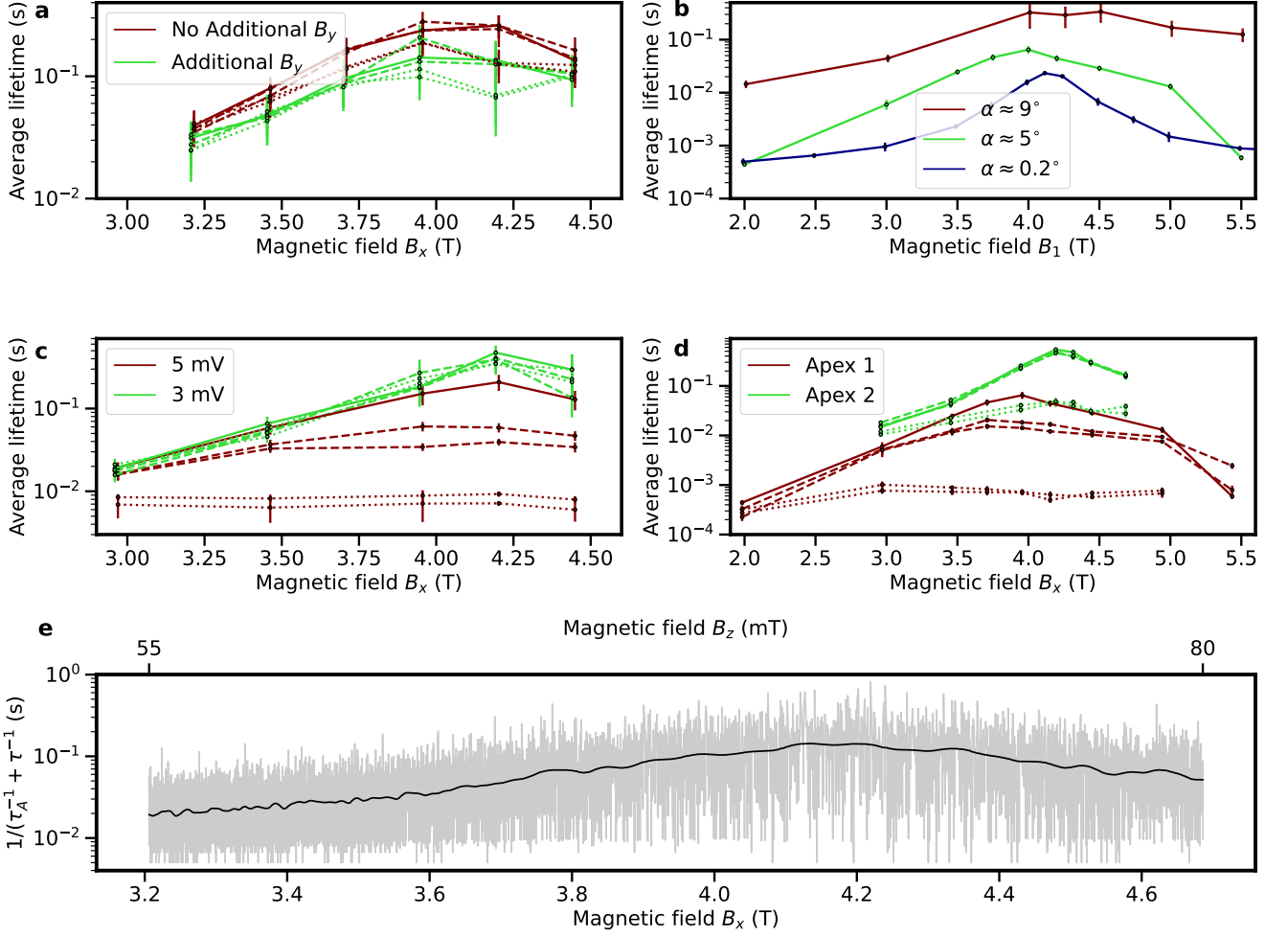


FIG. 7. Lifetime curves for antiferromagnetic Fe_5 under various experimental conditions. (a) Lifetimes measured for each Fe atom in the chain at different out-of-plane fields, B_y . The variation in B_y is primarily achieved by adjusting the B_2 field. For the green curves, $B_2 = \sin(8^\circ)B_1$, while for the red curves, $B_2 = 0$. (b) Lifetimes measured for atom III at different α values obtained by rotating the crystal. The labels indicate the actual angle. The data in the main text (Fig 2d) is included in blue. (c) Lifetimes for each Fe atom in a chain measured at different bias voltages. (d) Lifetimes measured under the same conditions on the same chain but using two different tips. (e) Up-to-up switching time, defined as $1/(1/\tau_A + 1/\tau_B)$ (gray), while sweeping the external magnetic field from 4.75 T to 3.25 T. During the sweep, the tip remained in constant-current mode over the atom III to compensate for drift. The time between switches was long enough such that the tip height followed telegraphic noise-like behaviour. A rolling average of 50 points is given in black. All magnetic field values, B_x and B_z , were determined by converting the applied external magnetic fields considering the crystal axes. All data (except for the blue curve in (b) and the green curve in (c)) were obtained with $V_{\text{bias}} = 5$ mV, $I = 10$ pA, $T = 1.3$ K (blue data obtained at $T = 1.4$ K and $V = 3$ mV). All data (except the red and blue curves in (b)) were obtained with $\alpha = 5^\circ$. Error bars represent 2 standard deviations. Connecting lines between data points are guides to the eye. Solid lines correspond to atom III, dashed lines to atoms II and IV, and dotted lines to atoms I and V.

To clarify major effects of B_y (Fig. 7a), α (Fig. 7b), V_{bias} (Fig. 7c) and tip apex (Fig. 7d) on the shape of the lifetime curves, we present further data sets obtained under various conditions on an antiferromagnetic Fe_5 chain. Further analyses of voltage dependence, as well as current dependence, are explored in Supplementary Notes 7 and 8, respectively.

As explained in the previous section, although the external magnetic fields \mathbf{B}_1 and \mathbf{B}_2 are closely aligned along the in-plane and out-of-plane directions, respectively, simultaneous adjustments of \mathbf{B}_1 and \mathbf{B}_2 are necessary to selectively apply a field along one of \hat{B}_x , \hat{B}_y and \hat{B}_z . For instance, applying \mathbf{B}_1 to change the in-plane field induces a finite out-of-plane field, given by $B_y = B_1 \sin(8^\circ)$. To understand the effect of the out-of-plane magnetic field on the lifetime, we varied \mathbf{B}_2 in a way to double the total B_y experienced by the chain, i.e., $B_2 = B_1 \sin(8^\circ)$. As shown in Fig. 7a, the overall lifetimes show a slight reduction, and the peak near the diabolic point is slightly attenuated with increased B_y , consistent with simulations. Although a more thorough analysis is required, we expect that fully compensating B_y could yield slightly more pronounced peaks near the diabolic point. However, since the influence of B_y is not substantial and a small B_y would not change the underlying physics behind our studies, we kept $B_2 = 0$ for the rest of our experiments.

Adjusting the angle α is correlated with changing the ratio between two in-plane fields, B_x and B_z . A larger α corresponds to a higher B_z at a certain B_1 . The increase in B_z is associated with an increasing contribution of the main Néel states for ψ_0 and ψ_1 , at the expense of the minor contribution. In other words, $\psi_0 \rightarrow N_A$ and $\psi_1 \rightarrow N_B$, leading to a reduction in hybridization. Thus, at a larger α , we observed an overall increase in the lifetime compared to a smaller α . Secondly, the Zeeman splitting between these two lowest-lying states was increased, which results in the smearing out of the peak near the diabolic point (Fig. 7b). Note that the lifetime curves were measured with different samples and different tips since we needed to remount the crystal to rotate it and thus to change α , which may introduce additional effects of local environments on the chain, such as local defects, strain in the underlying Cu_2N layer, diverse tip apexes, and so on. The influence of different tip apexes is shown in Fig. 7d. As measured on the same Fe_5 chain but with different spin-polarized tips, the lifetime varies not only in the magnitudes but also in the magnetic field value for the lifetime peak. This indicates variations of the tip magnetic fields along both B_x and B_z .

Figure 7c shows the effect of the applied bias voltages. Increasing the voltage results in more over-the-barrier transitions and, thus, larger variations in the lifetime among the atoms in the chain (consistent with the data shown in Fig. 3a of the main text). See also Supplementary Notes 8 and 9 for further discussions.

Figure 7e shows the up-to-up switching times during a magnetic field sweep. The raw data is given in gray, while the black line shows a rolling average using SciPy's 1D Gaussian filter (50 data points). Even for this rough measurement, we can clearly see the switching rate is significantly reduced near 4.15 T, corresponding to the diabolic point. Considering that obtaining a dataset for lifetime curves takes at least one day, this 45-minute measurement provides a quick way to verify the location of the diabolic point.

SUPPLEMENTARY NOTE 5: SYMMETRY BREAKER OF Fe_6

In the absence of external magnetic fields, the two lowest-lying eigenstates, ψ_0 and ψ_1 , in an Fe chain are composed of the symmetric and antisymmetric superposition of the Néel states, respectively. The energy difference between these states arises from transverse magnetic anisotropy ($E(S_x^2 - S_y^2)$). This energy difference is effectively mitigated by applying a transverse magnetic field B_x . At the diabolic point, the B_x fully compensates for the energy difference, leading to an energy level crossing. In an ideal situation, where all atoms on a surface are identical and devoid of any variations in local environments, the diabolic point is expected to manifest in an exceedingly sharp window of B_x (a singular point value) with nearly infinite lifetimes. This sharp transition can be smeared out by converting the level crossing into an avoided-level crossing, where the broadening is proportional to the energy difference between the two states.

For a ferromagnetic chain or an odd-numbered antiferromagnetic chain, this avoided-level crossing can be easily induced by applying a longitudinal magnetic field B_z , which yields the energy difference between two Néel states by the Zeeman energy. In contrast, achieving an avoided-level crossing for an even-numbered antiferromagnetic chain is nontrivial, as the two Néel states possess identical energies across all B_z fields. This conflicts with our observations from the Fe_6 chain in Fig. 3a, which suggests a symmetry break between the two Néel states, ultimately making one state more favored than the other under a finite Zeeman energy. We attribute this symmetry break to inhomogeneity in the chain. In reality, there are subtle variations in local environments among atoms on surfaces, which results in different g -values and magnetic interactions between them. In addition, the presence of a magnetic tip located over one atom in the chain provides a tip-induced local magnetic field.

In our simulations, the Zeeman energy induced by variations in g -values is included by assigning a different g -value to atom I in the chain rather than introducing varied g -values for all atoms. Consequently, the total Zeeman splitting is proportional to an applied field along the \hat{z} -axis and the g -factor mismatch between the atom I and the rest of the atoms $g_1 - g_{\text{rest}}$.

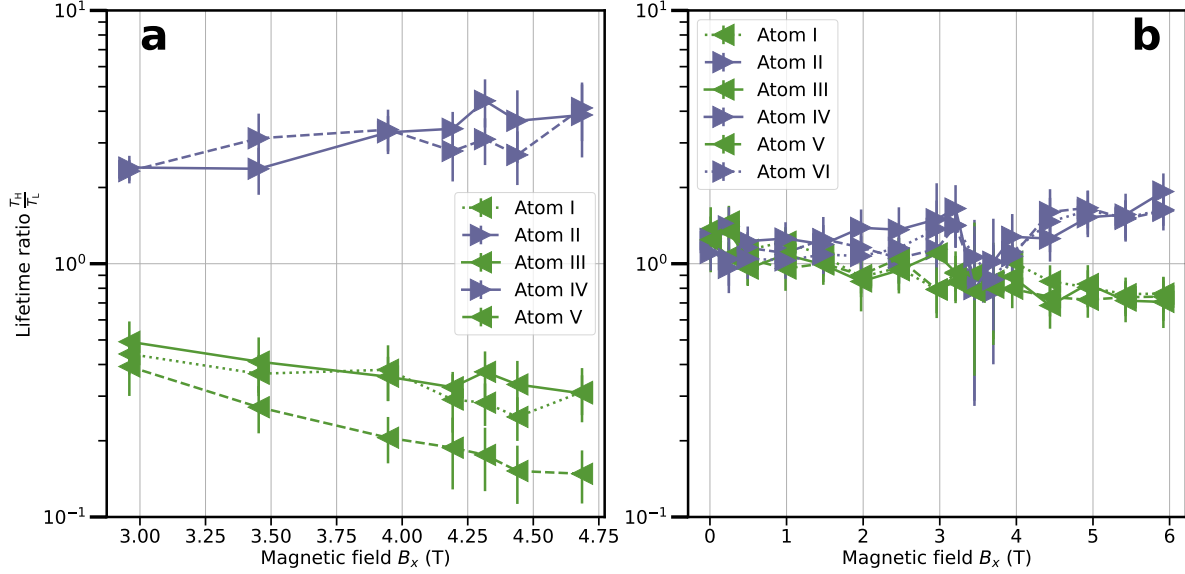


FIG. 8. **Lifetime ratios defined as T_H/T_L for odd- and even-numbered chains.** (a) Lifetime ratios of a Fe_5 chain obtained at $\alpha = 5^\circ$. In the chain, even-numbered atoms II and IV exhibit a lifetime ratio of about 3, while odd-numbered atoms I, III, and V show a lifetime ratio of about $1/3$ across the given magnetic field range. (b) Lifetime ratios of Fe_6 for the data presented in the main text. Blue and green colors indicate even- and odd-numbered atoms, respectively. A split between even- and odd-numbered atoms starts to emerge around 2 T, diminishes around the diabolic point, and increases for higher magnetic fields. Lines are guides to the eye. Error bars represent two standard deviations. Data in panel a corresponds to the 10 pA data presented in Fig. 12.

To confirm the symmetry break, we compare the lifetime ratios between atoms in the Fe_5 and Fe_6 chains. While our primary focus in the main text is on T_A and T_B for the average lifetimes associated mostly with Néel states N_A and N_B , respectively, we shift our attention here to the average lifetimes of T_H and T_L related to high and low spin-polarized current states, respectively. This keeps the analysis more general and highlights the alternating pattern of antiferromagnetic chains better. At the diabolic point, in the absence of Zeeman energy, the two lowest-lying states are degenerate, resulting in equal lifetimes for T_H and T_L (i.e. $T_H/T_L \approx 1$). Importantly, this means that a larger imbalance between T_H and T_L indicates a greater energy difference between the two states. Thus, we use the lifetime ratio T_H/T_L as a proxy for the ratio of state ensemble occupation, which, according to the Boltzmann distribution, provides insights into the energy difference between the two states.

Figures 8a and b present the lifetime ratios (T_H/T_L) for the Fe_5 and Fe_6 chains, respectively. In the Fe_5 chain, the lifetime ratio for atoms I, III and V is about $1/3$, while for atoms II and IV, it is about 3. This simple inversion in the T_H and T_L ratios indicates that ψ_0 and ψ_1 predominantly consist of specific Néel states, namely N_A and N_B , respectively. Interpreted as population ratios, the lifetime ratios given in Fig. 8a correspond to an energy difference between ψ_0 and ψ_1 of about $140 \mu\text{eV}$ at around 4T. Note that this dataset was obtained with the sample's angle of $\alpha \approx 5^\circ$, which is larger than the one in Fig. 2.

The Fe_6 chain (Fig. 8b) shows relatively small variation in the lifetime ratios among the atoms. As mentioned before, in an ideal situation, the even-numbered AFM chain should yield $T_H/T_L = 1$. However, as shown in Fig. 8b, especially at larger B_x values, a finite splitting occurs. We attribute this splitting to slight variations in the g -factors of the atoms arising from local imperfections near the atoms, such as defects or edges of the Cu_2N island (indicated by white arrows in STM images of Fig.9). For $B_x < 2$ T, the lifetime ratios measured on each atom are approximately the same, albeit slightly larger than unity. We interpret this as the result of a longitudinal tip field of about 30 mT causing a similar imbalance on each atom. Around the diabolic point (3.5 T), the lifetime ratios approach unity. Meanwhile, at $B_x = 6$ T, the lifetime ratios are about 1.6 and 0.70 for even- and odd-numbered atoms in the chain, respectively. This corresponds to an energy difference of about $50 \mu\text{eV}$, which clearly indicates the Zeeman energy between two ground states induced due to the inhomogeneity among atoms in the chain.

SUPPLEMENTARY NOTE 6: INVESTIGATING α_{tilt}

While the crystal orientation with respect to the STM stage (α_{atomic}) can be estimated by scanning the sample surface at atomic resolution, the alignment between the STM stage and the magnets need to be thoroughly investigated to identify the

magnetic fields with respect to the crystal axes. When applying B_1 , the B_z field expressed in the crystal axes is given by $B_z \approx B_1 \sin(\alpha)$. Due to a slight misalignment ("tilt") between the magnetic field axes and the STM stage, the angle α_{atomic} , derived from atomic resolution topographic images, needs to be corrected by a value α_{tilt} such that the angle $\alpha = \alpha_{\text{atomic}} - \alpha_{\text{tilt}}$. Note that α_{tilt} remains constant throughout our experiments, set by the installation of the STM stage with respect to the magnets, while α_{atomic} varies depending on how the substrate is mounted on the sample holder. In this section, we demonstrate that $\alpha_{\text{tilt}} = 3^\circ$, estimated from the analysis of lifetime ratios and peak widths of lifetime curves.

The peak width of a lifetime curve and the lifetime ratios primarily depend on the energy difference between ψ_0 and ψ_1 , dominated by the Zeeman energy. Accurate determination of the Zeeman energy necessitates the determination of the angle α , considering α_{atomic} and α_{tilt} . In our experiments, crystal orientations can be adjusted by rotating the sample with respect to the sample holder. Figures 9a–f show lifetime ratios and corresponding STM images for three different chains, each with a different α_{atomic} . From STM images, we can extract the angle α_{atomic} for each of the chains: $\alpha_{\text{atomic}} = -2^\circ$ for Fig. 9b, $+3^\circ$ for Fig. 9d, and $+12^\circ$ for Fig. 9f. Depending on α_{atomic} , we observe clear variations in the lifetime ratios and in their deviations between even- and odd-numbered atoms of the chains due to different Zeeman energies. For $\alpha_{\text{atomic}} = 3^\circ$ (Fig. 9c), we observe a negligibly small difference in lifetime ratios between even- and odd-numbered atoms, which already implies the minimal Zeeman energy ($\alpha \approx 0$). Based on the extracted angle α_{atomic} , we deduce B_z values relative to applied magnetic fields B_1 and, thus, calculate Zeeman energies for each chain. For a single unpaired spin with $S = 2$ for the Fe_5 chain, the Zeeman energy is given by $\Delta E \approx 4g\mu_B B_z \approx 4g\mu_B B_1 \sin(\alpha)$. We subsequently calculate lifetime ratios based on the populations of ψ_0 and ψ_1 through the Boltzmann distribution at the Zeeman energy and $T = 1.8$ K, slightly exceeding the measurement temperature of $T = 1.3 \sim 1.4$ K (see also Table II).

Assuming $\alpha_{\text{tilt}} = 0$ (thus, $\alpha = \alpha_{\text{atomic}}$), the calculated Zeeman energies and corresponding lifetime ratios are depicted by yellow shading in Fig. 9a,c,e. We found substantial deviations between our measured values and the calculated Zeeman energies for $\alpha_{\text{tilt}} = 0$, which suggests the influence of a nonzero α_{tilt} and variations in the g -factors among the chain's atoms. As discussed in Supplementary Note 5, we consider the inhomogeneity of g -values by assigning a distinct g -factor to atom I, differing from the rest ($g_{\text{rest}} = 2.11$ following literature [10]). To optimize g_1 and α_{tilt} , we initially assume $\alpha_{\text{tilt}} = 0$ and adjust g_1 to scale the calculated Zeeman energies, aligning them with our results. Subsequently, we fine-tune α_{tilt} to compensate the scaling by g_1 to keep g_1 within a reasonable range. To characterize both odd- and even-numbered chains uniformly, we introduce the concept of "unpaired spins". For an ideal Fe_5 chain ($g_1 = g_{\text{rest}}$), there would be one unpaired spin with uncompensated Zeeman energy. Conversely, in an ideal Fe_6 chain, no unpaired spins would be present. However, considering inhomogeneity ($g_1 \neq g_{\text{rest}}$), the unpaired spin for antiferromagnetically coupled even-numbered chains is defined as $(g_1/g_{\text{rest}} - 1)$.

To match the calculated Zeeman energies with our experimental results, we adjust the values of unpaired spins (i.e., g_1). We found optimal agreement when we set the unpaired spins as 4.25, 0.1, and 0.65 for Fig. 9a,c, and e, respectively, while keeping $\alpha_{\text{tilt}} = 0$. This is shown in orange shading. Next, we try to compensate for an offset of the angle, α_{tilt} , to bring the number of unpaired spins in all measured odd chains as close to unity as possible. This adjustment is carried out as follows: Fig. 9g shows the determined number of unpaired spins with $\alpha_{\text{tilt}} = 0$ (bottom) and with $\alpha_{\text{tilt}} = 3^\circ$ (top). The overall values of unpaired spins are much closer to 1 for $\alpha_{\text{tilt}} = 3^\circ$. Note that the angles (α) used for the simulations in the main text all lie within an error margin of 1 degree compared to the measured angles, after accounting for the tilt ($\alpha_{\text{tilt}} - \alpha_{\text{atomic}}$). Note also that outside of this Supplementary Note α will always be presented as $|\alpha|$.

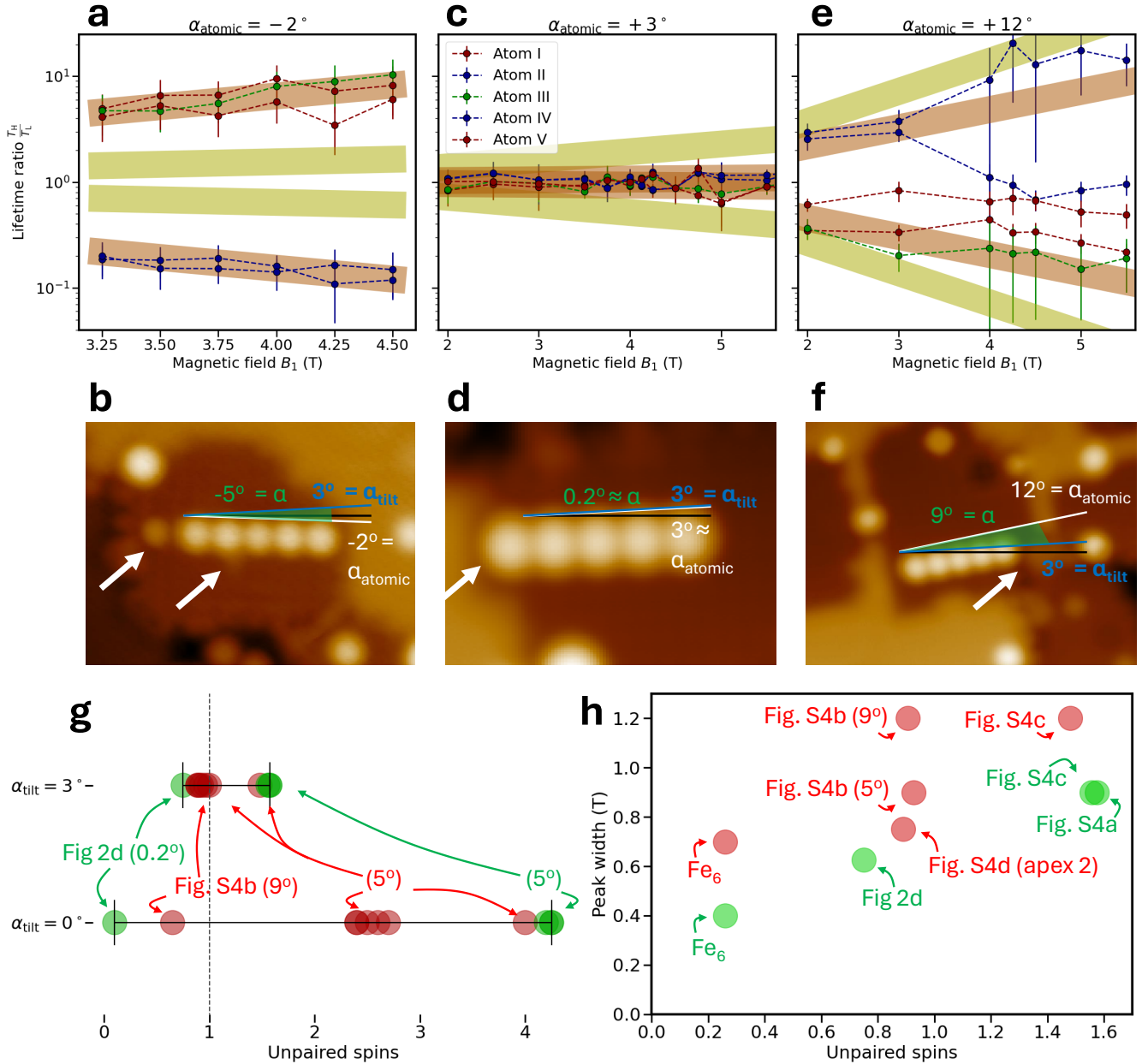


FIG. 9. Determining crystal axes. (a) Lifetime ratios T_H/T_L and (b) STM image for the Fe₅ chain. The corresponding lifetime curve for this chain is given in red in Fig. 7a. The atomic resolution image presents $\alpha_{\text{atomic}} = -2^\circ$. Considering the Zeeman energy of one “unpaired spin” for the Fe₅ chain, the calculated lifetime ratios at this angle are represented by the yellow shading, where $\alpha_{\text{tilt}} = 0^\circ$ and g -factors are homogeneous between atoms. However, our measurement shows 4.25 times larger Zeeman splittings, as indicated by the orange shading. (c,d) Same as (a,b), but $\alpha_{\text{atomic}} = +3^\circ$. The corresponding lifetime data are shown in Fig. 2d. For $\alpha_{\text{atomic}} = +3^\circ$, the measured Zeeman energy (orange shading) is now 0.1 times smaller than the calculated Zeeman energy (yellow shading). (e,f) Same as (a,b), but $\alpha_{\text{atomic}} = +12^\circ$. The corresponding lifetime curve is shown in a red curve in Fig. 7b. The lifetime ratios given from the measurement show the Zeeman energy is 0.65 times smaller than the calculated value. Arrows given in each STM image indicate nearby defects that may cause symmetry breaking. The angle $\alpha = \alpha_{\text{tilt}} - \alpha_{\text{atomic}}$ is given for $\alpha_{\text{tilt}} = +3^\circ$. (g) Overview of all determined unpaired spins throughout this work before (“ $\alpha_{\text{tilt}} = 0^\circ$ ”) and after (“ $\alpha_{\text{tilt}} = 3^\circ$ ”) adjusting the angle α_{tilt} . (h) Overview of unpaired spins and peak width for the various data sets throughout this work. The peak width for atom III is defined as half the range of B_x values over which the lifetime is at most one order of magnitude smaller than the peak lifetime. For panels g and h: Green circles indicate data taken at $V_{\text{bias}} = 3$ mV, red circles taken at 5 mV. Inserted labels indicate the correspondent dataset and the angle α .

Lastly, using the adjusted tilt angle $\alpha_{\text{tilt}} = 3^\circ$ and the corresponding calculated Zeeman energies in terms of unpaired spins, we show the peak width for several different Fe chains as a function of unpaired spins in Fig. 9h. The green and

red symbols indicate data taken at 3 mV and 5 mV, respectively. For the latter, we need to consider over-the-barrier transitions, thereby leading to a slight reduction in peak height and an increase in peak width. This effect is clearly observed in the data for Fe₆ and the data presented in Fig. S4c. Furthermore, an increase in Zeeman energy (through an increase in unpaired spins or angle) is also associated with a larger peak width, as expected. Note that the data in Fig. 2d was obtained at a much smaller angle than the rest of the dataset in this overview, resulting in a smaller Zeeman energy.

Despite the Fe₅ chain having an estimated Zeeman energy of around 30 μeV , it is surprising that the peak width in Fig. 2d is somewhat larger than that of the Fe₆ chain with a Zeeman energy of about 50 μeV . Given the very small energy difference between ψ_0 and ψ_1 for the data in Fig. 2d, we did not find any convincing indicator to associate the low current in Fig. 2a with Nèel state A. Without loss of generality we picked this based on Fig. 2b and c, where, for the specific case of $B_x = 4$ T, the average lifetime of the low current state is longer than the average lifetime of the high current state. Code for processing all the lifetime ratios is available in the Open Data folder.

SUPPLEMENTARY NOTE 7: LIFETIME OF THE FE₃ CHAIN

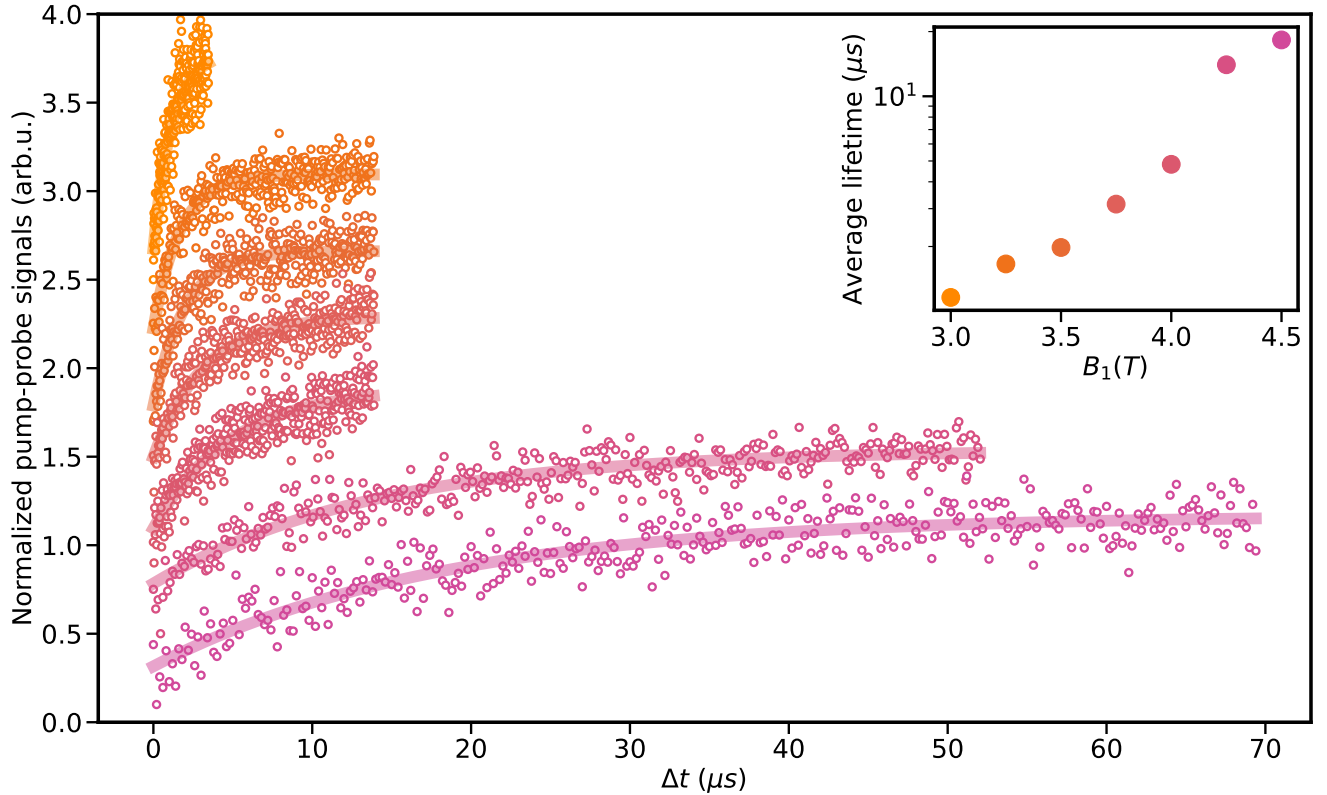


FIG. 10. **Pump and probe measurements for the Fe₃ chain at different B_x fields.** Pump-probe signals measured on the center atom of an Fe₃ chain at different B_x magnetic fields. Considering the crystal axes with respect to the magnets' axes, increasing the B_1 results in increasing both B_x and B_z in a way of $B_z \approx 0.09 \cdot B_x$. With increasing B_x , we found the lifetimes monotonically increase (see inset). For the Fe₃ chain, our simulation shows the diabolic point (almost) exceeding our magnetic field range. Setpoint: $V_{\text{DC}} = 10$ mV, $I = 200$ pA, $V_{\text{pump}} = 35$ mV, $V_{\text{probe}} = 5$ mV, and $T = 1.3$ K. Each pump and probe measurement is offset for clarity.

SUPPLEMENTARY NOTE 8: VOLTAGE DEPENDENCE OF LIFETIMES

To identify the regimes for the quantum tunneling of magnetization (QTM) and over-the-barrier transitions, we measured the spin lifetimes of Fe_5 chains as a function of bias voltages. At bias voltages corresponding to electron energies below the magnetic anisotropy barrier (i.e. less than the energy of ψ_2), to first approximation, we expect the lifetimes to be constant, while above the barrier the lifetimes are expected to decrease gradually. Figure 11a shows the average spin lifetimes of an antiferromagnetically coupled Fe_5 chain. Below 4 mV the spin lifetime is constant with bias, indicating the QTM regime. Above 4 mV, spin lifetimes of the outer atom decrease as bias increases. This threshold voltage appears higher for the inner atoms. Due to this variation of threshold voltages between the atoms in the chain, the lifetime curves given in Fig. 3a show strong dependence on the atoms when measured at 5 mV. This observation can be understood by larger values of J_i and D_i further towards the center of the chain, see also Supplementary Note 1. Additionally, owing to the nodal structure of excitation modes, the next lowest excited energy states (e.g. ψ_2) are expected to be primarily localized on the outer atoms [14].

In Fig. 11b, we show analogous data for the ferromagnetically coupled Fe_5 chain. The blue and black circles present the results measured at the same conditions as in Fig. 11a for the central and outer atoms, respectively. Here we clearly observe a maximum lifetime at around 3 mV. This feature likely emerges as a consequence of increased tip-chain exchange interactions at lower bias voltages, which decreases the spin lifetimes. To keep the tip-chain interaction constant, we fixed the conductance to ~ 6.6 nS and repeated the lifetime measurements at different voltages as given by faint blue and black squares in Fig. 11b. In this constant height measurement, we found a plateau of the lifetimes below ~ 3.5 mV. Unlike the antiferromagnetic chain, the threshold voltages for the over-the-barrier transitions are similar between the atoms in the chain. Thus, for both antiferromagnetic and ferromagnetic chains, we chose 3 mV to characterize the spin lifetimes due to the quantum tunneling of magnetization near the diabolic point.

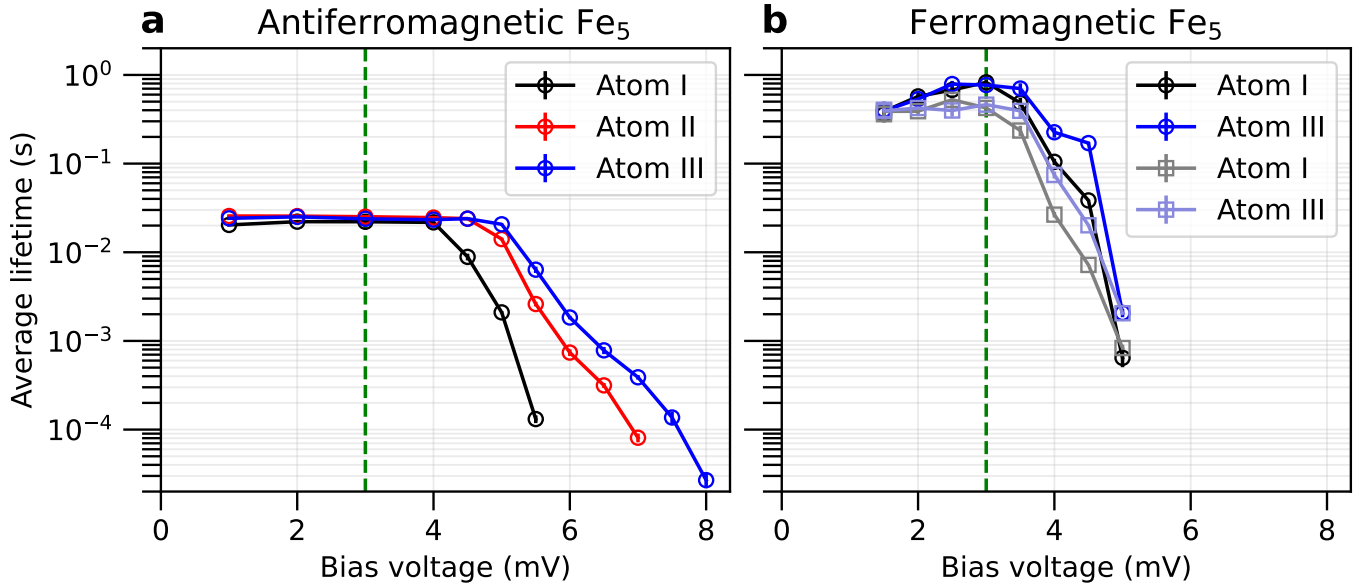


FIG. 11. **Voltage threshold for over-the-barrier transitions.** (a) Bias dependence of spin lifetimes for the antiferromagnetically coupled Fe_5 chain presented in Fig. 2d of the main text measured under constant-current mode at 10 pA. The measurements are shown for three atoms (I–III) in the chain. (b) Bias dependence of spin lifetimes for the ferromagnetically coupled Fe_5 chain presented in Fig. 3b. The blue and black circles show the data measured at a constant current of 10 pA. Faint blue and black squares represent the data obtained at a constant tip height (6.6 nS). Lines connecting data points are guides to the eye. The error bars (2σ) are smaller than the marker size. All data was obtained at $T = 1.4$ K, $B_x = 4.125$ T near the diabolic point for (a) and $B_x = 4.75$ T near the second diabolic point for (b).

SUPPLEMENTARY NOTE 9: CURRENT DEPENDENCE

In this section, we consider the effects of the current (I) on the lifetime of the antiferromagnetic Fe_5 chain. Figure 12 shows the lifetimes measured on each atom in the chain at different currents. Note that the bias voltage was set to 5 mV, at which

lifetime reductions due to over-the-barrier transitions become apparent, most notably on the outer atoms. We thus consider two separate transition rates: R_T for transitions due to tunneling of magnetization and R_O for over-the-barrier transitions. With increasing current, the lifetime generally decreases, due to both R_T and R_O increasing linearly with I . The lifetimes can be expressed in terms of transition rates: $(T_{\text{avg}})^{-1} \propto R_O + R_T = Ir_O + (I_0 + I)r_T = I(r_O + r_T) + I_0r_T$, where the coefficients r_O and r_T are based on the amplitudes of the scattering paths and I_0 is the current from the bath interacting with the chain, which has too little energy to induce over-the-barrier excitations. Note that r_O and r_T are independent of I but may be dependent on V_{bias} , T , atom location in the chain (i), and magnetic fields. We found that r_O does not depend on the transverse magnetic field, but r_T does.

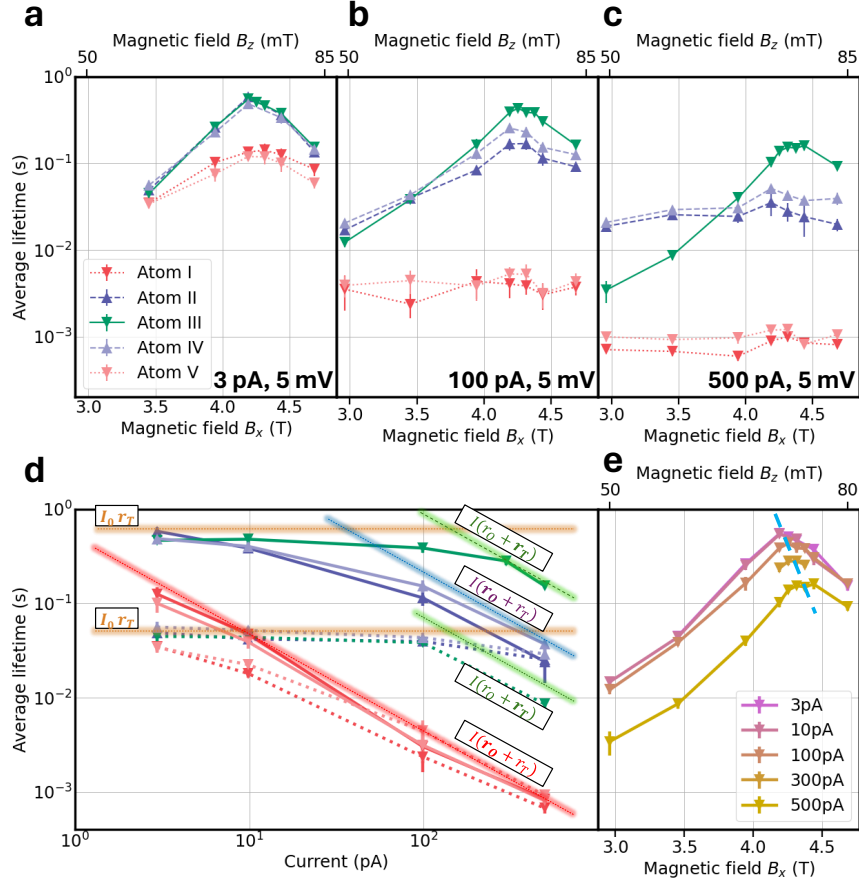


FIG. 12. **Current dependence of spin lifetimes.** (a) Lifetimes measured on each atom at 3 pA, (b) 100 pA, and (c) 500 pA. All data was taken at 5 mV and $T = 1.3$ K. Associated B_z is shown on the top axes. Lines are guide to the eye. Error bars are 2σ . (d) Lifetimes of each atom as a function of current at $B_x = 3.5$ T (dotted) and at the first DP $B_x^{5,1}$ (solid). Dashed glowing lines represent lifetimes calculated considering transition rates. (e) Lifetimes of atom III as a function of magnetic fields at different currents. The blue dashed line indicates $B_x^{5,1}$ used in (d) corresponding to the magnetic fields of the maximum of lifetimes.

Figures 12a–c show the lifetimes measured for each atom in the Fe_5 chain at a current of 3 pA, 100 pA and 500 pA, respectively. When increasing the current, the outer atoms show no signature of a diabolic point, as R_O becomes too large. In contrast, the diabolic point remains visible for atom III but appears at higher magnetic fields with overall reduced lifetimes (Fig. 12e). The dashed blue line in Fig. 12e indicates the shift of the DP as a result of the tip field. Increasing the current leads to smaller tip-sample distances and larger tip fields, resulting in the DP at larger external magnetic fields. This indicates that the tip field is counteracting the external magnetic field. Note that this corresponds to tip 2 of Fig. 7d. Importantly, atom III, not limited by over-the-barrier transitions, shows that the tip field does not destroy the appearance of the diabolic point, despite the field being applied to only one atom of the chain. This further supports the claim that this effect is robust to many variations in the parameters of the Hamiltonian.

This current dependence is further analyzed in Fig. 12d by plotting the lifetimes as a function of current at each magnetic field of $B_x = 3.5$ T (dotted lines) and $B_x = B_x^{5,1}$ (solid lines). We found four different effects of the current on the lifetimes:

1. As indicated by the orange lines in Fig. 12d, for the inner atoms, the lifetimes are nearly constant for smaller I , where

the plateau value and the threshold current depend on B_x . At the plateaus, the lifetimes are mostly determined by $I_0 r_T$, which depends on the scattering intensity and, thus, on B_x . Consistent with the rest of this work, in the absence of over-the-barrier transitions, a longer lifetime is observed at B_x closer to the DP.

2. Excitation over the barrier due to an applied bias and finite temperature causes R_O to limit the lifetime for all atoms [42]. At $V_{\text{bias}} = 5$ mV and $T = 1.3$ K, this effect is less significant towards the center of the chain (see Supplementary Note 8). This effect does not depend on field and should therefore result in constant lifetimes throughout the full range of B_x . This is the case for atoms I/V in Figs. 12b,c and atoms II/IV in Fig. 12c. This contribution scales linearly with current, as depicted by the red and blue glowing straight lines in Fig. 12d.
3. Additional electrons might cause through-the-barrier transitions if the electrons do not have enough energy to cause over-the-barrier transitions. We find that for the experimental conditions for Fig. 12, only atom III shows this behavior, as the shape of the lifetime curves in Figs. 12a–c does not really flatten with increasing current. These transition events also depend on the scattering amplitude between the lowest energy eigenstates. In Fig. 12d, this is highlighted with the green glowing dashed lines, which intersects with the orange lines at around 200 pA. This suggests the rate of bath electrons interacting with the system is of a similar order.
4. In Fig. 12c, the lifetimes of atoms II/IV appear higher than atom III for $B < 3.75$ T, which can be attributed to the atomic exchange bias as the magnetic tip approaches close to the chain at higher current. This exchange bias can be modeled as an increased B_z for atoms II/IV and a decreased B_z for atoms I/III/V in their ground state [16]. For $B > 3.75$ T, the lifetimes of atoms II/IV are limited by over-the-barrier transitions, while the atom III is free from this and, thus, shows longer lifetime.

SUPPLEMENTARY NOTE 10: METHODS AND DATA ACQUISITION

Sample Preparation

We used a home-built STM system [41], operating at 1.3 K and $B = 0 - 6$ T in the plane of the sample, mainly perpendicular to the axis of the chain. The $\text{Cu}_2\text{N}/\text{Cu}(100)$ sample was prepared as described in [15]. The tip was prepared as in [13]. Fe atoms on the Cu_2N were picked up by applying voltage pulses of ~ 1 V (setpoint of 100 pA, 20 mV, then moved -300 pm), and dropped at -600 μV with the tip gradually approaching the surface until an abrupt change in current was observed. The Fe was subsequently hopped into place with a pulse of ~ 1 V at (100 pA, 20 mV). Preferred hopping directions were determined by straining of the Cu_2N lattice in line with previous works [43], and utilized for efficient construction of the chains.

Data Acquisition

The spin-polarized STM tip was prepared by attaching several Fe atoms to the Cu-coated tip apex. Using this spin-polarized tip, the magnetization switching was measured in either a constant-current or constant-height mode. To measure the switching in the order of a millisecond or below, a DAQ (NI 782258-01) was used to record an incoming current stream of up to 10 seconds with the feedback turned off with a sampling rate of 10 kHz. For slightly longer lifetimes, the data was recorded directly through the internal DAQ of Nanonis electronics with a sampling rate of 2 kHz. For lifetimes longer than 100 ms, the feedback was turned on with an extremely long time constant in the feedback loop. This allows the feedback to account for drift, but keep the switching signals in the current data stream. For very long lifetimes (≥ 1 s), a constant-current mode was used such that the variation of tip heights was used to determine the magnetization switches. The tip's feedback was set such that the response time is much faster than the average switch time. The gradual drift of the tip height was subtracted from the data. The angle α was derived from the angle determined by atomic resolution STM images, and adjusted to include a tilt of 3° , see Supplementary Note 6.